9-9-2016

Computational Design of Ceramic Bone Scaffolds Fabricated Via Direct Ink Writing

Jeffrey Roberge
University of Connecticut - Storrs, jeffrey.roberge@uconn.edu

Computational Design of Ceramic Bone Scaffolds Fabricated Via Direct Ink Writing

Jeffrey Raymond Roberge

B.S., University of Connecticut, 2013

A Thesis

Submitted in Partial Fulfillment of the

Requirements for the Degree of Master of Science

at the

University of Connecticut

2016

Approval Page

Master of Science Thesis

Computational Design of Ceramic Bone Scaffolds Fabricated Via Direct Ink Writing

Presented by

Jeffrey Raymond Roberge, B.S.

Major Advisor_____

Dr. Julián Norato

Associate Advisor_____

Dr. Horea Ilieş

Associate Advisor_____

Dr. Mei Wei

University of Connecticut

2016

Acknowledgments

I am very grateful to my advisor Dr. Julián Norato for his continual support without which this thesis would not have been possible. He not only patiently guided my research and motivated my academic studies, but is a role model and inspiration academically and otherwise.

I would like to thank Dr. Ilieş and Dr. Wei for introducing me to the utility of CAD systems and the subtleties of biomaterials, respectively, and for their support of my project as part of my defense committee.

A special thanks goes to the Structural Optimization Laboratory, where Shanglong Zhang, Manal Tahhan, Hesaneh Kazemi, and Tyler Luneski were not only a source for brilliant ideas but of friendship too.

Dr. Moreno deserves thanks for helping me assimilate to graduate school and for supporting my research and career endeavors.

Thanks goes to Tom Mealy for 3D printing our more complicated geometries even when he was inundated with requests from the senior design class.

I owe thanks to my parents for always being there for me and trusting in my decisions, for nurturing my love of learning, and for all of the care packages that got me through school.

Thanks goes to Maggie Sadowski for her advice and valuable help in editing and creating figures for this thesis in addition to being someone I could always rely on especially in the last few stressful months.

Lastly, I would like to thank my friends who have always been there for me.

Contents

1 Introduction **1**
- 1.1 Motivation . . . 1
- 1.2 Objective . . . 3
- 1.3 Method Summary . . . 4
- 1.4 Outline . . . 6

2 Effective Materials Properties Model **7**
- 2.1 Introduction . . . 7
- 2.2 Cellular Solids Theory . . . 7
  - 2.2.1 Introduction to Cellular Solids . . . 7
  - 2.2.2 Applications . . . 8
  - 2.2.3 The Cellular Solids Method . . . 9
- 2.3 Numerical Homogenization . . . 13
  - 2.3.1 Introduction to Numerical Homogenization . . . 13
  - 2.3.2 The Numerical Homogenization Method . . . 13
  - 2.3.3 Cellular Solids Model Calibration . . . 15
- 2.4 Effective Properties Model for the Bone Scaffold . . . 16
  - 2.4.1 Bone Scaffold RVE . . . 16
  - 2.4.2 Assumptions . . . 16
  - 2.4.3 In-Plane Longitudinal Modulus . . . 17
  - 2.4.4 Shear Modulus . . . 19
  - 2.4.5 Poisson's Ratio . . . 20
- 2.5 Numerical Calibration of the Bone Scaffold . . . 22
  - 2.5.1 Computational Design of Experiments . . . 22
  - 2.5.2 Least Squares Nonlinear Regression . . . 31

3 Scaffold Design **35**
- 3.1 Design Requirements . . . 35
- 3.2 Existing Computational Scaffold Design Methodologies . . . 35
- 3.3 Proposed Design Method . . . 37
- 3.4 Optimization Problem Statements . . . 38
  - 3.4.1 Compliance minimization . . . 38
  - 3.4.2 Volume fraction minimization . . . 39
- 3.5 Sensitivity Analysis . . . 39
- 3.6 Design for Manufacturing . . . 42

3.7 Design Examples 45
3.7.1 Axial Loading Test 45
3.7.2 Comparison to Topology Optimization Code 47
3.7.3 Compliance Minimization of a Mandible Implant 48
3.7.4 Porosity Maximization of a Mandible Implant 52
3.8 Discussion 55

4 Conclusion **56**
4.1 Contributions to Bone Scaffold Technology 56
4.2 Future Research 56

Bibliography **57**

List of Figures

1-1 Direct ink writing of a ceramic scaffold [29] 5
1-2 Lattice fabricated using direct ink writing [28] 5

2-1 Examples of cellular solids: (a) a honeycomb, (b) an open-celled foam and (c) a closed-celled foam [30]. 8
2-2 Far-field stress applied to a honeycomb 10
2-3 RVE of a cubic foam undergoing a far-field shear stress 11
2-4 RVE of a 3D printed bone scaffold 17
2-5 Beam bending of an RVE rod (adapted from [37]) 19
2-6 Poisson's ratio effect within the RVE 21
2-7 Geometry projection representation (right) of a bar ω upon a fictitious domain Ω (left) 23
2-8 The sampling window for a finite element used to compute the element density in the geometry projection 24
2-9 Projected geometry of bone scaffold RVE 25
2-10 Flow chart to perform automated homogenization of all RVEs of table 2.1 using MPI for Python 26
2-11 Result of the 504 computational design of experiments, showing the entire numerical data set for G_{xz}/G_s versus porosity 27
2-12 Flow chart to perform homogenization of an RVE using ABAQUS 28
2-13 ABAQUS mesh representing a bone scaffold RVE of $\alpha = .15$ and $d/l = .1$ . . 29
2-14 RVE in ABAQUS showing all multipoint constraint equations 30
2-15 Von Mises contour plot of an RVE with $\alpha = 0.15$ and $d/l = 0.1$ for applied test strains: (a) $\epsilon_{11} = 1$; (b) $\epsilon_{22} = 1$; (c) $\epsilon_{33} = 1$; (d) $\epsilon_{12} = 1$; (e) $\epsilon_{13} = 1$; and (f) $\epsilon_{23} = 1$. 31
2-16 Analytical (lines) versus geometry projection (points) porosity as a function of d/l for different overlap ratios α. 33
2-17 In-plane effective shear modulus versus d/l for $\nu = 0.3$ and various α overlap ratios 33
2-18 In-plane effective Poisson's ratio versus d/l for $\nu = 0.3$ and various α overlap ratios 34
2-19 In-plane effective longitudinal modulus versus d/l for $\nu = 0.3$ and various α overlap ratios 34

3-1 (a) [44]; (b) [45]; (c) [46]; (d) [47]; (e) [20]; (f) [48]; (g) [49]; (h) [19]. 37
3-2 Adjacent level sets of Φ with a spacing of l from each other 43

3-3 (a) The boundary conditions and loads on a square uniform mesh creating axial deformation; (b) optimized scaffold, with arrows indicating the rod direction and arrow size representing d/l; (c) projected rod layout calculated using the level set method; (d) final geometry represented in FreeCAD . . . 46
3-4 Plot shows the boundary conditions and loads on a uniformly meshed square bone scaffold . . . 47
3-5 Optimized bone scaffold showing d/l and ψ for each finite element . . . 48
3-6 Objective function and constraint history for the short cantilever design example . . . 49
3-7 Density-based topology optimization of the short cantilever beam . . . 49
3-8 Boundary conditions for the bone scaffold (white) within a mandible (gray) example [53] . . . 50
3-9 Maximal stiffness design of a mandibular implant: (a) quiver plot of optimal ψ and d/l; (b) level sets of d/l; (c) rod directrices determined by level-set method; (d) final CAD geometry. . . . 51
3-10 Objective and constraint function history for the stiffness example . . . 52
3-11 Maximal porosity design of a mandibular implant: (a) quiver plot of optimal ψ and d/l; (b) level sets of d/l; (c) rod directrices determined by level-set method; (d) final CAD geometry. . . . 53
3-12 Objective and constraint function history for the maximal porosity example 54
3-13 Final geometry constructed by the Formlabs Form 1+ . . . 54

Abstract

Bone scaffold porosity and stiffness play a critical role in the success of critical-size bone defect rehabilitation. In this work, we present a computational procedure to design ceramic bone scaffolds to provide adequate mechanical support and foster bone healing. The scaffolds considered in our study consist of a lattice of curved rods fabricated via direct ink writing. We develop cellular solids models of the scaffold's effective elastic constants as functions of its geometric parameters, up to some unknown coefficients. To determine numeric values for these coefficients, we execute a computational design of experiments whereby effective elastic properties are obtained using numerical homogenization with the finite element method. In order to automate these experiments and circumvent re-meshing for every scaffold geometry, we project a representative volume element of the scaffold onto a fixed uniform mesh and assign an ersatz material for the analysis. Then, through a nonlinear least-squares regression, we fit the cellular solids models to the data set generated in this manner. Once calibrated, we use these models in conjunction with efficient gradient-based optimization methods to design patient-specific scaffolds (i.e., shape, location, and loading) by varying geometric parameters that can be controlled in the fabrication, namely the separation between rods in the lattice, and the orientation of the tangent vector to the rod axis. The optimization procedure renders element-wise values of rod separation and tangent vector orientation. As this representation is not amenable to fabrication, lastly, we generate the final scaffold geometry by posing a differential equation whose solution is a function such that its level set lines at specified values correspond to the directrices of the rods in the scaffold. We explore two problem formulations: maximization of stiffness of a mandible implant with a constraint on porosity, and maximization of porosity with a stiffness constraint equivalent to the stiffness of the bone native to the defect site.

Chapter 1

Introduction

1.1 Motivation

Critical-size bone defect prevalence is burgeoning with an expanding yet ageing population, requiring natural or synthetic bone grafts for correction. A bone graft is a general term coined to define a surgical procedure to place a bone or synthetic material into an existing defect or traumatic injury to facilitate rehabilitation. In 2010, there were more than 4,000,000 of these bone graft procedures performed annually across the world [1]. These commonly stem from traumatic injury, tumor resection, congenital defects, and infection or inhibited bone regeneration from conditions such as avascular necrosis or osteoporosis. Although the most common bone injury is a fracture, which is typically cured without invasive intervention (and less commonly with conventional methods such as plates, screws and pins to minimize bone non-union), there are oftentimes cases in orthopaedic, maxillofacial, and oral surgery where defects become too expansive to heal on their own [2]. This is where bone grafts become paramount. For example, ameloblastomas, juvenile ossifying fibromas, giant cell tumors, and traumatic injury (among others) are accompanied with a significant loss of bone. In the case where the defect is too large to heal without intervention, a load-bearing structure is needed to fill the defect space, return function to the site and provide a network to shape the healing bone. Currently, expansive mandible reconstruction is dominated by solid titanium prosthetics, but this precludes the opportunity for bone regeneration. A porous graft on the other hand, provides mechanical support to return normal function to the defect site and also acts as a bioreactor for cells and growth factors to expedite bone repair. Ideally, the defect site will return to natural bone.

Conventionally, bone grafts are harvested from the patient (autograft), from a donor (allograft), or from an animal (xenograft), however these methods are limited in availability. Autografts provide lower quality graft material due to limited vestigial bone donor sites, and burden the patient with donor site morbidity and additional surgical complications. Furthermore, allografts and xenografts can incite an immunogenic response and pose a threat through disease transmission [3, 4, 5, 6]. To circumvent these issues, synthetic bone grafts, or scaffolds, have become prominent in recent years. They are designed as an artificial bone matrix, capable of hosting growth factors, cells and in-growth of native tissues. Cellular and growth factor scaffold considerations are outside of the scope of this work and are

subsequently ignored henceforth. Materials and fabrication processes have been developed to replicate native bone structure and defect shape while retaining manufacturability.

To fully understand the materials, structure and subsequent success of these bone implants, it is important to understand bone physiology. Bone is a mechanically complex structure that is composed of an organized mineral component, hydroxyapatite (HA), and a tough fibrous component, type-I collagen [7]. Osteoblasts continually build an interwoven mesh of collagen which is mineralized with HA to form bone. Osteoclasts conversely resorb bone to contribute to a constant bone reformation that ultimately arranges bone, particularly the porous, medially located trabecular (cancellous) bone [7], to minimize compliance along axes of principle stress [8]. Bone thus has an inherent regenerative capacity that is capitalized on to allow for bone graft osteointegration (implant fixation to bone), osteoconduction (bone growth onto a surface) and osteoinduction (osteogenesis stimulation) to enhance the efficacy of bone grafts [9].

Since bone scaffolds aim to accommodate bone formation for implant adhesion and consequently success, most bone scaffolds adopt a highly porous and otherwise bone-like morphology. Scaffolds require an open-pored, interconnected structure with pore sizes between 150-900 μm [10]. Porosity allows for proper angiogenesis (the development of new blood vessels), nutrient transport and waste removal while concurrently fostering osteoconduction. This osteoconduction is critical for osteointegration and the subsequent success of implants, especially within craniofacial applications [9].

To meet these criteria, metal, polymer and ceramic based scaffolds have been introduced. Traditional implants for load-bearing cortical bone defects are metallic, bioinert solids due to their higher modulus and hardness. Modern implants use rapid prototyping or casting techniques to make porous osteoconductive scaffolds, but first they must be modified to enhance surface characteristics [1]. Without surface alteration, metals have low levels of biological compatibility. With techniques such as Direct Metal Laser Sintering (DMLS) or Electron Beam Melting (EBM), intricate porous internal structures can be created in stainless steel, AlSi10Mg, Inconel 625, Inconel 718, Ti-6Al-4V, and CoCrMo among others [11]. Other fabrication methods such as gas injection into melted metal, templated vapor deposition, and self propagating high temperature synthesis also provide porous structures, but these methods lack the ability to control pore geometry, pore connectivity and total porosity [12]. With metals, the scaffold may remain exceedingly load-bearing over the lifetime of the implant. Consequently, the surrounding bone will see substantially less load than healthy bone. Since osteocyte stimulation and the subsequent osteoblast activation depend on the mechanotransduction induced by the load, the surrounding bone will cease to grow and recede, a phenomenon known as stress shielding [12, 5]. Alternative scaffold materials have been researched to avoid this issue.

Polymer scaffolds are widely diverse and offer greater biocompatibility, workability, and degradability than metals. Polymer scaffolds can be harvested from natural sources, that exhibit enhanced biocompatibility such as collagen, although these may not preclude foreign body response and disease transmission. Polymer scaffolds can be synthesized, in which case their degradation rate can be controlled by molecular design, with the implant success contingent on matching the polymer degradation rate with that of bone growth [13]. The most researched of these synthetic materials are the polyesters poly(glycolic acid) (PGA), poly(lactic acid) (PLA) and poly(lactic-co-glycolic acid) (PLGA) [14]. While chosen for

their good mechanical strength and tuneability, degradable polymers suffer from acidification under degradation and potentially harmful byproducts. Like metal scaffolds, they generally need surface modification to enhance osteoconduction. Fabrication techniques render various levels of porosity, interconnected pore size and, in general, architectural control, leading to varying degrees of osteoconductivity. Techniques range from little architectural control, such as emulsion freeze-drying and gas-foaming processes, to those with high control, such as 3D printing, whereby an ink-jet printer lays a binder on top of respective powder layers [13], or direct ink writing, whereby deposition of colloidal or otherwise polymer-based inks create 3D structures [15].

Ceramics are another type of scaffold material that while strong, are limited by current processing techniques. Alumina, bioactive glass, HA and β-tricalcium phosphate (β-TCP) are common examples of bioceramics used in scaffold technologies. Alumina is dense and mostly inert so that fixation within the bone is not through osteoconduction, but through morphological fixation (press-fitting) [16]. On the opposite end of the spectrum, HA is bioactive and osteoconductive in itself, owing to the fact that it already is a major component in the crystalline portion of natural bone. Through fabrication, the porosity of the ceramic base material can be controlled and used to lower its modulus compared to bone. Current ceramic scaffold preparation methods range from those with poor geometry control such as chemical foaming, sintered microsphere, and pore forming methods, to high geometry control, such as direct ink writing (also known as robocasting [15] or μ-robototic deposition [17]), stereolithography appearance, and selective laser sintering [18]. The latter methods can create interconnected and controllable porous structures. Despite the increased architectural control offered by these fabrication techniques, typical scaffold designs are periodic and therefore they are not structurally optimal from a stiffness and porosity point of view. Moreover, other than the outer contour, which must fit the shape of the defect, they are not patient-specific.

The interplay of cancellous bone and cortical bone provides a mechanically variegated structure that proves exceedingly difficult to recreate using existing scaffold fabrication techniques. However, the architectural control provided by some of the aforementioned techniques can be further exploited by designing scaffolds tailored to the shape and loading of individual defects so as to, for example, maximize bone ingrowth while retaining load-bearing capacity and preventing stress shielding. Such personalization of the scaffold design will result in greater biological integration [19, 20, 21, 22].

1.2 Objective

The objective of this thesis is to develop a computational procedure to design optimal, patient-specific ceramic bone scaffold fabricated via direct ink writing to maximize the porosity of the scaffold while approximating the stiffness of the bone native to the defect region. The latter stiffness goal will lead to reduced stress shielding, while the former porosity goal will increase osteoconduction and thus promote osteointegration. Our computational methodology is tailored to direct ink writing as this technique provides reasonable control of the architecture of ceramic scaffolds so as to control their stiffness and porosity. Specifically, our method should render designs that are readily translated to manufacturing.

1.3 Method Summary

In this thesis we present an efficient method to design printed biocompatible ceramic (for instance, HA) scaffolds in order to maximize porosity given a stiffness requirement. As aforementioned, bone scaffolds need to be porous in order to allow for proper osteoconduction and osteointegration. Typical trabecular bone, also known as cancellous bone, exhibits a rod- and plate-like microstructure that follows the orientation of the principal stresses [23, 8]. To emulate this configuration, in this work we consider a lattice structure made of alternating layers of rods such as the one depicted in figure 1-1c. By controlling the layout of the ceramic rods, we can control the porosity while trying to emulate the stiffness of the bone that would otherwise occupy the defect. Ultimately this will reduce stress shielding, increase osteoconduction and decrease the likelihood of implant failure [16, 24, 25].

We focus on ceramic scaffolds because they exhibit an inherent osteoinductivity, more so than that of metal (which otherwise needs surface modification) [26, 27], and have stiffness higher than that of polymer counterparts and hence they have greater load-bearing capacity. Also, we focus on the aforementioned lattice configuration because the layout of the rods can be accurately controlled using solid free-form fabrication. In particular, we consider scaffolds made via direct ink writing. In this technique, a 3-dimensional (3D) printer with a cylindrical extrusion nozzle lays rods of a colloid following a computer aided design (CAD) model, as depicted in figure 1-1. Layers are deposited transversely, creating joints at the intersections. A periodic scaffold made by this technique is shown in figure 1-2. A variety of print parameters including printer head speed, calcination time of the powder, colloid composition, and nozzle size determine the final lattice geometry. Subsequent sintering solidifies the scaffold and makes the joints fully effective [28]. This lattice system creates a load-bearing structure that, thanks to the porosity and the biocompatibility and stiffness of the ceramic, provides a suitable environment for bone ingrowth, osteoconduction, and bioactivity [16, 24, 25]. More importantly, the rods arrangement need not be periodic, and the local rod orientation and separation can be controlled on an individual scaffold basis via manufacturing. This design freedom creates a significant opportunity that we aim to exploit in this work, namely that we can design and fabricate patient-specific scaffolds so as to maximize osteoconduction while guaranteeing load-bearing capacity and preventing stress shielding. The patient-specific design derives from accounting for the size, shape, location and loading of the individual defect. Finally, we restrict ourselves to low-load, planar bones such as the mandible, since existing biocompatible ceramics are not strong or stiff enough to serve as implants in long, high load-bearing bones.

At the heart of our method is the use of cellular solids models to establish relationships between a scaffold's periodic geometry and the bulk ceramic elastic properties, and the scaffold effective moduli. These cellular solids models lead to functional expressions with unknown constants. We determine these constants by calibration via a computational design of experiments, whereby we perform numerical homogenization of a representative volume element (RVE) of the scaffold subject to periodic boundary conditions to obtain effective properties for different scaffold geometries. We then perform regression via non-linear least squares to fit the cellular solids models to these numerical experiments and determine the unknown constants. This calibration results in closed-form relationships between the scaffold's effective moduli and its geometric parameters that can be used for designing the scaffold.

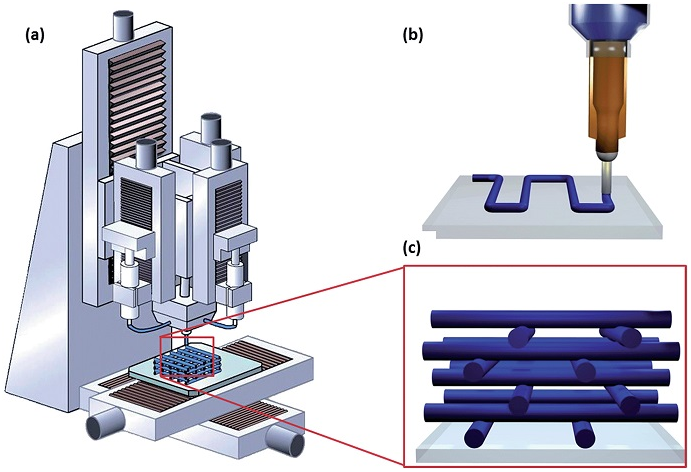

Figure 1-1: Direct ink writing of a ceramic scaffold [29]

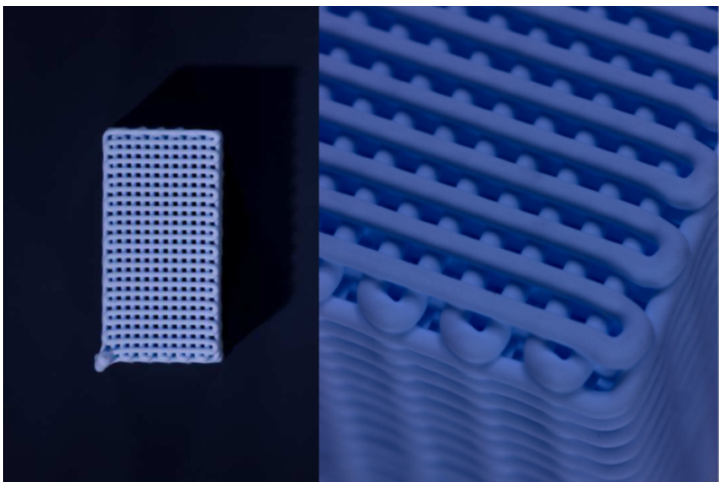

Figure 1-2: Lattice fabricated using direct ink writing [28]

The advantages of employing mechanics-based cellular solids models as opposed to naive numerical fitting to, e.g., polynomial models, are a reduced number of fitting constants and increased fitting accuracy over a wide range of parameter values owing to the fact that the form of these models is obtained from the deformation of the unit cell.

Once cellular solids models of the scaffolds effective properties are available, we model the implants using finite element analysis. To this end, we mesh the bone defect to be replaced by the implant and its surrounding bone structure using continuum elements whose properties equal the effective properties of the RVE. Specifically, the elasticity tensor of the elements in the implant is obtained as a function of the scaffold's geometric parameters, such as the ratio d/l, where d is the rod diameter and l is the rod separation. Furthermore, by rotating the elasticity tensor in each finite element, we can accommodate the design of scaffolds whose rods are curvilinear. Therefore, our design variables for the optimization correspond to the d/l ratio and the rod orientation ψ at, e.g., each element centroid. Since these are closed-form expressions, we can obtain analytical design sensitivities of the porosity

and stiffness and therefore employ efficient and robust gradient-based optimization methods for the design. The optimization therefore renders values of d/l and ψ for each element in the implant mesh. To translate these into a scaffold layout that can be fabricated via direct ink writing, we formulate and solve a differential equation whose solution is a continuous field such that specified level set lines of this field correspond to rods in the desired layout.

The novelties of this work consist of developing the first patient-specific design methodology for this material system, namely a ceramic bone scaffold fabricated by direct ink writing. Our methodology conforms to the manufacturing process by establishing closed-form relationships between the scaffold's geometric parameters (which can be readily controlled by the process) and its effective properties as well as by direct translation of the optimal design into a layout ready for fabrication. Also novel is the coupling of ('off-line') cellular solids models[1] with gradient based optimization to drive the design.

There are several limitations which bound the scope of this work. We do not consider compressive strength or stability in the design. We also do not take into account the time-dependent change in stiffness caused by bone tissue adaptation or scaffold resorption, but instead focus solely on the most mechanically demanding conditions–those seen during initial implantation. For simplicity, we only consider planar bones with in-plane loading and in doing so we use the cellular solids model which assumes a periodic layout, however, the scaffold design is not periodic. Likewise, we do not consider edge effects between the implant and the surrounding bone and assume a perfect bond between scaffold and bone. Furthermore, details such as the effect of the variability in the loading, bulk ceramic properties, and dimensions of the scaffold on the porosity and stiffness are omitted. In considering these limitations, it is clear that there is ample room for further development beyond the scope of this work.

1.4 Outline

Chapter 2 describes the derivation of the cellular solids models of the scaffold's effective properties as functions of its geometric parameters. This description includes the execution of a computational design of experiments, whereby numerical homogenization for a number of scaffold geometries is performed to determine unknown constants in the cellular solids models. Chapter 3 details the proposed scaffold design methodology, which uses the foregoing cellular solids models coupled with gradient-based optimization to efficiently produce maximal stiffness and maximal porosity scaffolds. This chapter also describes the development of a level set-inspired methodology to translate the result of the optimization into a solid geometry that can be directly sent to a format suitable for fabrication. A benchmark problem and two mandibular implant design exercises are presented. Finally, in chapter 4, conclusions are drawn, highlighting accomplishments, shortcomings, and potential future endeavors.

[1] As opposed to 'on-line' models such as numerical homogenization, which must be updated upon each design change during the optimization

Chapter 2

Effective Materials Properties Model

2.1 Introduction

In order to control the scaffold's porosity and stiffness, these quantities need to be expressed as functions of the scaffold's design parameters. In this work, we accomplish this using cellular solids theory. A bone scaffold with a grid layout such as that described in the previous chapter is expected to be orthotropic. Since in this work we only consider implants for planar bones, we only need to characterize the properties of the scaffold on the plane of the grid. In what follows, we briefly describe the principles of cellular solids theory, and we apply them to determine expressions for the effective elastic constants as functions of the scaffold design up to some unknown coefficients. Finally, we use numerical homogenization and the geometry projection method to perform a computational design of experiments to determine the unknown coefficients.

2.2 Cellular Solids Theory

2.2.1 Introduction to Cellular Solids

The term cellular solids derives from the word cell, which implies a small enclosure. In particular, cellular solids theory studies the effective properties of 2-dimensional (2D) or 3-dimensional (3D) assemblages of these cells. Cells may appear as closed structures with membranous walls or open structures with interconnected struts [23, 30]. Figure 2-1 shows some examples of cellular solids.

An important property of a cellular solid is its relative density, defined as the cellular density divided by the solid density. Porosity, on the other hand, is given by the subtraction from unity of the relative density. It has been shown that the effective mechanical properties of many naturally occurring and man-made cellular solids can be expressed as functions of the relative density [23, 30], hence this is an important quantity to describe a cellular solid. In general, cellular solids are considered to be only those whose relative density does not exceed 0.3 [23, 30].

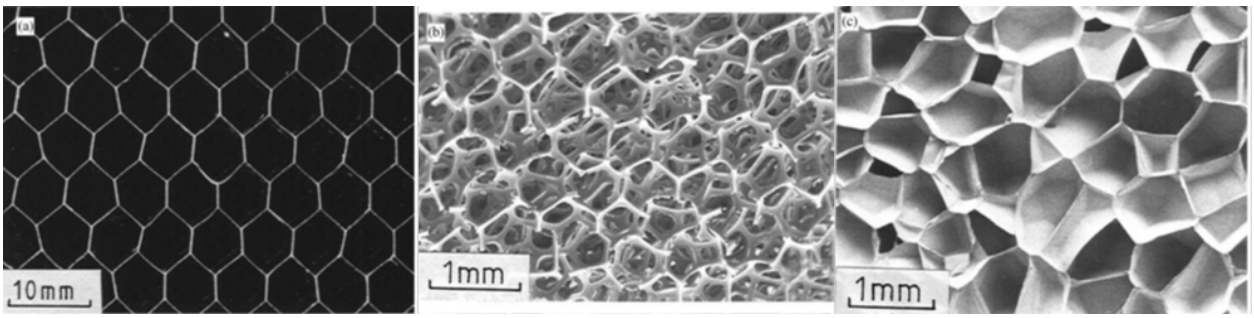

Figure 2-1: Examples of cellular solids: (a) a honeycomb, (b) an open-celled foam and (c) a closed-celled foam [30].

2.2.2 Applications

Found in society as early as 5000 years ago in the form of Egyptian wood structures, cellular solids are as ubiquitous as they are archaic. Cellular solids are also abundantly found in nature. For example, trees have a prismatic honeycomb assemblage of cells that gives rise to flexural and axial stiffness [23, 30]. Plant leaves exhibit sandwich structures where a dense exterior surrounds a porous cellular interior. This is also seen in skull bones, where cortical bone (the dense exterior) and cancellous bone (the porous interior) impart strength and rigidity while remaining lightweight. Cork is another example of a cellular material whose closed-cell structure once made it a useful boat hull material.

Increasingly, man has created synthetic cellular solids for several applications. As with wood, cellular solids have many structural applications. For example, man-made sandwich panels in the aircraft industry, usually made of aluminum or paper honeycombs covered by carbon fiber-reinforced face sheets, give rise to bending stiffness and noise reduction [23]. Foamed titanium has seen a structural application in cancellous bone replacement.

Applications of cellular solids are not limited to structural applications. Cellular solids have also seen uses in thermal insulation, buoyancy and filtration among others. Foams exhibit a low thermal conductivity, so they have been used with success in refrigeration, kilns, and natural gas transports [23]. Foams can absorb large amounts of energy without accruing excessively high stress and so they see applications in packaging materials. Closed-cell structures with a density far below that of water are used to impart buoyancy in boats or flotation devices. Open-celled foams have seen success in filtration, and even in material delivery. For example, a catalytic converter is a honeycomb which is coated in platinum [23], whereby the honeycomb delivers the platinum catalyst to the exhaust system.

In order to characterize and design cellular solids, we need to establish relationships between the scaffold geometry and its properties. Moreover, we can use these relationships to model the behavior of the cellular solid by using a continuous, homogenized material as opposed to using a detailed model of the entire cellular micro-structure. This results in drastic computational savings, particularly in the context of design, since many analyses are typically required.

2.2.3 The Cellular Solids Method

Generally speaking, cellular solids theory consists of examining the deformation of a suitable spatial unit upon application of a far-field stress, which, after algebraic manipulation, leads to expressions of the cellular solid's effective properties as functions of its geometry. Here, we enumerate the steps of the method [23]:

1. Find the smallest unit whose behavior is representative of the cellular solid (the so-called representative volume element (RVE)). In the case of periodic cells, the RVE simply corresponds to a cell.

2. Apply a uniform far-field stress on the cellular solid.

3. Determine the equivalent loads and moments induced by the far-field stress on the RVE.

4. Find a representative deformation model of the RVE and of the whole cellular solid for the given loading.

5. Solve for the elastic property of interest by equating the deformation of the RVE to that of the bulk cellular solid. Typically, this effective property is expressed as a fraction of the corresponding elastic property of the material.

In what follows, we detail each one of these steps and provide an example of the application of the method.

2.2.3.1 Selection of an RVE

Here, we restrict ourselves to periodic cellular solids, such as the scaffold described in the previous chapters, cf. figure 1-2. The scaffolds we seek to design in this work are not periodic, and therefore we incur some error in the modeling of the elastic behavior of the scaffold. However, this assumption of periodicity allows us to establish an 'off-line' material model, leading to a very efficient design procedure. The alternative, i.e. to use an 'on-line' analysis model such as a finite element analysis with a mesh that conforms to the geometry of the entire scaffold, is not only substantially more expensive, but re-meshing upon changes in the geometry of the scaffold is a highly error-prone process that is difficult to automate.

For a periodic cellular solid, the RVE can be chosen as the smallest periodic cell.[1] If we assume that the RVE is much smaller that the overall dimensions of the cellular solid, and if we neglect edge effects, then imposing periodic boundary conditions on the RVE provides an accurate approximation of the elastic behavior of the cellular solid [31].

2.2.3.2 Application of Far-Field Stress

The next step to the method is to apply an appropriate far-field stress. A far-field stress is one which is applied distal enough as to not impose local stress concentrations. This assumption is implicit in the use of periodic boundary conditions on the RVE. The choice

[1] The choice is not unique, as one can shift the boundaries of the RVE and still obtain a periodic cell.

of the stress direction follows the effective elastic constant of interest. For example, if a longitudinal modulus in a given direction is sought for, a uniform axial stress in the same direction is applied. Figure 2-2 shows an example of a hexahedral honeycomb RVE with a far-field stress in the x direction. In this case, the far-field stress will result in the solution for E_{11}^*/E_s, where E_{11}^* is the effective modulus and E_s is the Young's modulus of the isotropic bulk material.

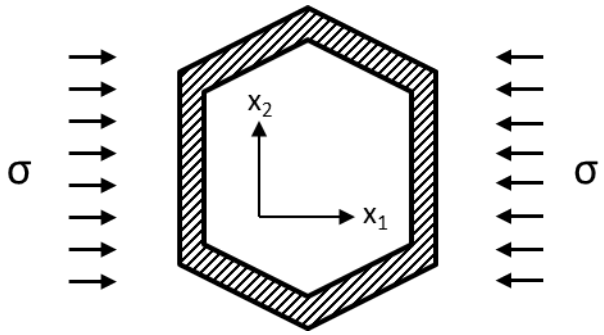

Figure 2-2: Far-field stress applied to a honeycomb

2.2.3.3 Determination of Loads and Moments

In this step, we determine how the far-field stress translates into loads and moments acting on the RVE. For example, in the case depicted in figure 2-2, the loading induced on the RVE by the applied far-field stress results in moments and concentrated loads in equilibrium on the vertices of the cell. The magnitude of this load, as illustrated in the subsequent examples, is determined by equilibrium.

2.2.3.4 Determination of a Deflection Model

This step consists of determining how the RVE will deform upon the applied loads. This is perhaps the most difficult step because trial and error of different deformation models is required until an accurate representation is found. The correct deformation model is determined by comparing the obtained effective properties for a range of RVE geometric parameters against experimental values, or against high-fidelity computational experiments using, for example, numerical homogenization. For simple RVE geometries, such as with the cubic foam example presented below, simple deflection models can be readily obtained. In that example, spars are long with regards to their thickness so that shear and axial effects can be neglected and simple Euler-Bernoulli beam bending can be assumed. In the case of closed-cell foams, plasticity, buckling, or more complicated geometries or behaviors, the deformation model is not so simple and finite element analyses may be required to determine the way in which the RVE deforms.

2.2.3.5 Determination of Effective Properties

To solve for the effective elastic property, we first relate the deflection of the geometric elements of the RVE (for example, the spars of figure 2-2) to the strain of the RVE. By com-

patibility of displacements, this strain equals the macroscopic strain of the cellular solid, and so by equating these expressions, and after algebraic manipulation, we obtain the effective elastic property typically as a fraction of the corresponding property for the bulk material. The following example elucidates this process.

2.2.3.6 Example: Effective In-Plane Shear Modulus of a Cubic Foam

In this example, we obtain the relative shear modulus of a cubic open-celled foam. We devised and provided this example due to its similarity to the calculation of the bone scaffold's shear modulus. Figure 2-3 depicts the undeformed and deformed shapes of a periodic RVE of the foam.

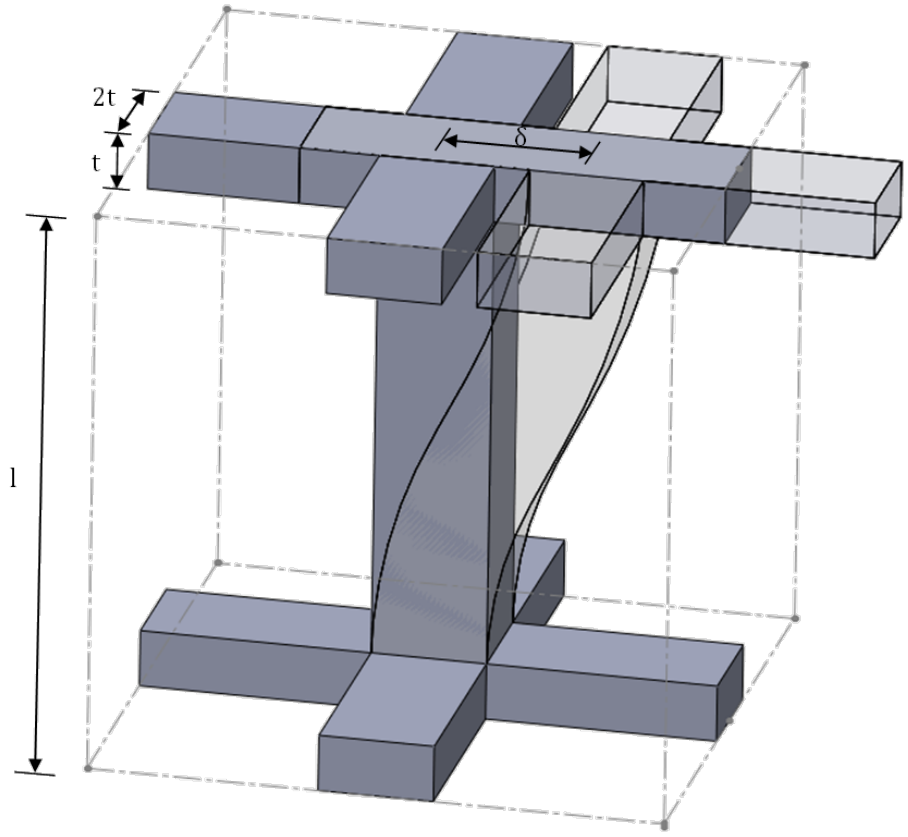

Figure 2-3: RVE of a cubic foam undergoing a far-field shear stress

Since we are seeking the relative shear modulus, the applied far-field stress must be a uniform shear stress. We assume that the deformation of the RVE for this loading will be dictated by bending of the vertical spar in the RVE. Therefore, the applied far-field shear stress would translate into a load F applied at the corners of the vertical spars. From equilibrium, this force is given by

$$F = \tau l^2 \tag{2.1}$$

The deformation γ of the macroscopic foam, which we assume behaves linearly elastic, can be inferred from Hooke's law:

$$\tau = \frac{G^* \gamma}{2} \tag{2.2}$$

At the RVE level, we relate the deformation γ of the RVE to the deflection of the vertical spar. The value δ determines the beam deflection, l is the spar length, and γ is the angle of deflection which also denotes the RVE shear strain. Since we assume the deflection to be within the linear elastic regime, and therefore deflections are infinitesimal, we find that

$$\gamma = \frac{\delta}{l} \tag{2.3}$$

This follows the small-angle approximation $\sin(\gamma) \approx \tan(\gamma) \approx \gamma$. The beam deflection can be readily obtained from Euler-Bernoulli beam theory as:

$$\delta_{max} = \frac{F l^3}{12 E_s I} \tag{2.4}$$

where I is the area moment of inertia of the vertical spar given by $I = t^4/12$. Combining equations (2.1)-(2.4), we find

$$\frac{\tau}{\gamma} = \frac{E_s t^4}{l^4} \tag{2.5}$$

where $\tau/\gamma = G^*/2$. Rearranging this expression yields

$$\frac{G^*}{E_s} = C_1 \left(\frac{t}{l}\right)^4 \tag{2.6}$$

where we have introduced an arbitrary constant C_1 to account for discrepancies incurred by our assumptions. The right-hand side of this expression is dimensionless, which we expect since we used continuum mechanics assumptions and hence the length scale does not matter. We can also express the relative shear modulus as a function of the relative density. To this end, we note that the volume of the cellular solid is given by

$$\rho^* = C_2 t^2 l \tag{2.7}$$

where we neglect the overlaps among spars [23] since their contributions to the volume are negligible for small t/l. The volume of the cell is given by

$$\rho = l^3 \tag{2.8}$$

Subsequently,

$$\frac{\rho^*}{\rho} = C_2 \left(\frac{t}{l}\right)^2 \tag{2.9}$$

Therefore, the relative shear modulus is given as a function of the relative density as

$$\frac{G}{E_s} = C_3 \left(\frac{\rho^*}{\rho}\right)^2 \tag{2.10}$$

2.2.3.7 Cellular Solids Conclusions

The cellular solids method leads to expressions of the effective properties of the cellular solid with respect to the cell geometry. However, these expressions contain unknown constants. In other words, these expressions provide the correct form of the dependence of the elastic properties on the cell geometry, but do not provide accurate predictions of the properties. Since we plan to use the cellular solids model as a predictive model for the scaffold design, the unknown constants need to be determined by curve fitting the cellular solids model to a numerical or experimental data set [23]. Here, we employ numerical homogenization to achieve this, as detailed in the following section.

2.3 Numerical Homogenization

2.3.1 Introduction to Numerical Homogenization

Homogenization is the averaging of the properties within an RVE of a complex microstructure to match that of the material seen on a macroscopic scale. This process simplifies the analysis of a specimen in the macroscopic scale by replacing the intricate microstructure with a solid homogeneous material whose properties represent in average the mircrostructure [32]. This method is carried out numerically by a finite element analysis of the RVE. It should be noted that numerical homogenization differs from mathematical homogenization. In the latter, purely mathematical techniques, such as asymptotic analysis [33], are used to obtain effective properties. However, these tools are generally confined to relatively simple RVE geometries, and are of no use for the scaffold geometry we study in this work.

2.3.2 The Numerical Homogenization Method

As in the cellular solids method, numerical homogenization is achieved by first determining the smallest RVE that is representative of the whole. Second, periodic boundary conditions are applied to simulate the RVE being in situ (or fully embedded in the material). Then, six unit test strains in 3D and three unit test strains in 2D are applied to the RVE [32, 34, 35]. In commercial finite element codes, these strains may be imposed as anisotropic, uniform unit thermal strains [34]. The applied 2D test strains are here denoted as ϵ_{11}, ϵ_{22}, and ϵ_{12}, and the additional 3D test strains are denoted as ϵ_{33}, ϵ_{23}, and ϵ_{13}. For each test strain, a finite element analysis is performed and the resulting stress fields are collected (σ_{11}, σ_{22}, σ_{33}, σ_{12}, σ_{23}, σ_{13}) as well as all of the resulting strain fields. These values are then used within the following equations to recover the homogenized constitutive tensor.

The numerically homogenized fourth-order stiffness tensor in component notation is com-

puted as

$$E^H_{ijkl} = \frac{1}{|V|}\int_V \left[E_{ijkl} - E_{ijpq}\frac{\partial \chi^{kl}_p}{\partial y_q}\right] dv \tag{2.11}$$

where χ^{kl} and $\partial\chi^{kl}_p/\partial y_q$ represent the displacement and strain respectively resulting from the application of the ϵ^{kl} test strain, and V is the domain occupied by the RVE [32]. This expression can be simplified into a more tractable notation that provides an easier transition to finite element implementation [32, 35]:

$$E^H_{ijkl} = \frac{1}{|V|}\int_V E_{pqrs}\left(\epsilon^{0(ij)}_{pq} - \epsilon^{*(ij)}_{pq}\right)\left(\epsilon^{0(kl)}_{rs} - \epsilon^{*(kl)}_{rs}\right) dv \tag{2.12}$$

where $\epsilon^{*(kl)}_{rs}$ denotes the resulting strain given by

$$\epsilon^{*(kl)}_{rs} = \frac{1}{2}\left(\frac{\partial \chi^{kl}_r}{\partial y_s} + \frac{\partial \chi^{kl}_s}{\partial y_r}\right) \tag{2.13}$$

and the ϵ^0_{ij} refer to the applied unit strain test fields [32, 35]. These unit strains are applied under periodic boundary conditions through, for example, nodal tying or imposition of multi-point constraints. Each unit strain leads to a finite element problem in the form

$$\mathbf{K}\boldsymbol{\chi}^{kl} = \mathbf{f}^{kl} \tag{2.14}$$

where $\mathbf{f}^{kl}$ and $\mathbf{K}$ are computed from the element e strain-displacement matrix $\mathbf{B}_e$, the bulk material elasticity matrix $\mathbf{E}$, and the test strains $\epsilon^{0(kl)}$:

$$\begin{aligned}\mathbf{f}^{kl} &= \sum_e \int_{v_e} \mathbf{B}^T_e \mathbf{E}_e \epsilon^{0(kl)} dv \\ \mathbf{K} &= \sum_e \int_{v_e} \mathbf{B}^T_e \mathbf{E}_e \mathbf{B}_e dv\end{aligned} \tag{2.15}$$

with v_e denoting the element e domain. Using this notation, equation (2.12) can be rewritten as

$$\mathbf{E}^H = \frac{1}{|V|}\sum_e \int_{V_e} \left(\mathbf{I} - \mathbf{B}_e\boldsymbol{\chi}_e\right)^T \mathbf{E}_e \left(\mathbf{I} - \mathbf{B}_e\boldsymbol{\chi}_e\right) dV_e \tag{2.16}$$

where $\mathbf{E}^H$ is the homogenized constitutive tensor, $\mathbf{I}$ is the identity matrix representing the unit strains, V_e is the domain of the current element e, and $\boldsymbol{\chi}_e$ is the matrix whose columns are the displacements corresponding to each of the applied test strains [35].

Another method to compute $\mathbf{E}^H$ that is simpler to implement is to compute E^H_{ijkl} as [34]:

$$E^H_{ijkl} = \frac{1}{|V|}\int_{V_e} \sigma^{kl}_{ij} dV_e \tag{2.17}$$

where σ^{kl}_{ij} are the stress influence coefficients defined as the stress fields induced by the unit test strains [34]:

$$\sigma_{ij}^{kl} = E_{ijmn}\left(\epsilon_{mn}^{*(kl)} + I_{mnkl}\right) \tag{2.18}$$

where $I_{mnkl} = (\delta_{km}\delta_{ln} + \delta_{lm}\delta_{kn})/2$ are the components of the fourth-order symmetric identity tensor $\mathbf{I}^{sym}$, with δ_{ij} the Kronecker delta function.

2.3.3 Cellular Solids Model Calibration

In order to calibrate the cellular solids method, i.e. to determine the unknown constants, we need to compare the effective properties of the RVE computed by cellular solids theory and numerical homogenization experiments. To gather a large enough data set to allow for an adequate comparison, the numerical homogenization procedure needs to be performed for a range of each of the material and geometric parameters. For instance, in section 2.2.3.6, the example provides the relative shear modulus as a function of t, l, and ν. A multi-level full factorial design may be used to this end [28].

Once a complete data set is amassed, a regression analysis is performed to find the optimal values of the unknown C_i's that minimize the error between the cellular solids model and the data set. Here, we employ the method of nonlinear least squares optimization whereby the sum of the squared residual is minimized by modifying the C_i [28, 36], i.e.:

$$\min_{\mathbf{C}} \sum_j \left(F(\mathbf{C}, xdata_j) - ydata_j\right)^2 \tag{2.19}$$

where $F(\mathbf{C}, xdata_j)$ is the property predicted by the cellular solids model for a given combination of parameters $xdata_j$ and a vector of unknown constants $\mathbf{C}$, $ydata_j$ is the 'observed' property in the numerical homogenization experiment performed with $xdata_j$, and $r_j = F(\mathbf{C}, xdata_j) - ydata_j$ is the residual for experiment j [36]. The unconstrained optimization problem of equation (2.19) is solved when the first order optimality condition is satisfied [36], i.e.:

$$\sum_j r_j \frac{\partial r_j}{\partial C_i} = 0 \tag{2.20}$$

In order to increase the possibility of finding a global minimum, different initial guesses of $\mathbf{C}$ should be attempted. Once the cellular solids model is fitted to the data set, the resulting constants $\mathbf{C}$ can be substituted into the model, at which point we no longer need the numerical homogenization method for our design methodology.

It should be noted that one could use the computational design of experiments and perform a regression with a number of approximation models, for example, polynomials, instead of using the cellular solids expressions. However, as demonstrated in [28] and in section 2.5.2, doing so leads to a larger number of calibration constants; but more importantly, even with a larger number of constants, the accuracy of the approximation is in general not as good as that of the cellular solids model because the form of the expression (e.g., a polynomial) may not correspond to the deformation of the RVE. Therefore, in comparison to generic response surface models, the cellular solids model is more compact and more accurate over a wide range of parameter values.

2.4 Effective Properties Model for the Bone Scaffold

In this section, we employ the foregoing techniques to obtain uncalibrated expressions for the longitudinal and shear moduli and the Poisson's ratio of the scaffold described in the previous chapter.

2.4.1 Bone Scaffold RVE

The structure in figure 2-4 depicts a single RVE of the 3D-printed bone scaffold (figure 1-2) that we will use for all derivations. The dotted line demarcates the boundaries of the RVE. The rod diameter, which is dictated by the deposition nozzle and therefore common to all rods in the scaffold, is here denoted by d. l is the distance between rods and it can be controlled by programming of the deposition pathway. As shown later, the relative porosity of the scaffold is proportional to d/l. The distance between the parallel midplanes of the rods is denoted by a, and it is given by

$$a \coloneqq d(1-\alpha) \tag{2.21}$$

where $0 < \alpha < 0.5$ is the fraction of the diameter of a rod that penetrates the rod in the underlying layer. This rod overlap ratio is caused by colloidal transverse rod integration, and it is not a parameter that can be readily controlled in the manufacturing. Nevertheless, as we will show in the sequel, it is still important in the derivation of the RVE's effective properties.

2.4.2 Assumptions

To develop our cellular solids models, we make several assumptions. As aforementioned, it is assumed that the cellular solids model of the periodic RVE adequately captures the local behavior of a scaffold with varying rod separation and orientation (i.e., one that has curved instead of straight rods).

We also do not account for more complex modes of failure such as plasticity, fracture, buckling, etc. The sintered rod joints are fully effective and linearly elastic.[2] The material used in the bone scaffold is isotropic and it behaves in the linear elastic regime. This material likewise is assumed to be extruded as a perfect cylinder with no bowing upon deposition or material contamination (such as with air bubbles).

The design parameters are bound to range within realistic or available values. The Poisson's ratio is limited to $\nu = [0.2, 0.35]$. The overlap ratio α is bounded as $\alpha \in (0.0, 0.5)$; the lower bound prevents pure contact between rods of adjacent layers, while the upper bound prevents pure contact of rods from two layers apart. The d/l ratio is bounded by $d/l \in (0.0, 1.0)$. The lower bound corresponds to an infinite separation between the rods, whereas the upper bound would allow contiguous rods in the same layer to come in contact. The former case would produce a vastly porous and unstable structure, while the latter case would render very low porosity and would hence not be useful as a scaffold. Therefore, here

[2]Note that rods are not in contact, but that have fully effective joints that are fused during sintering.

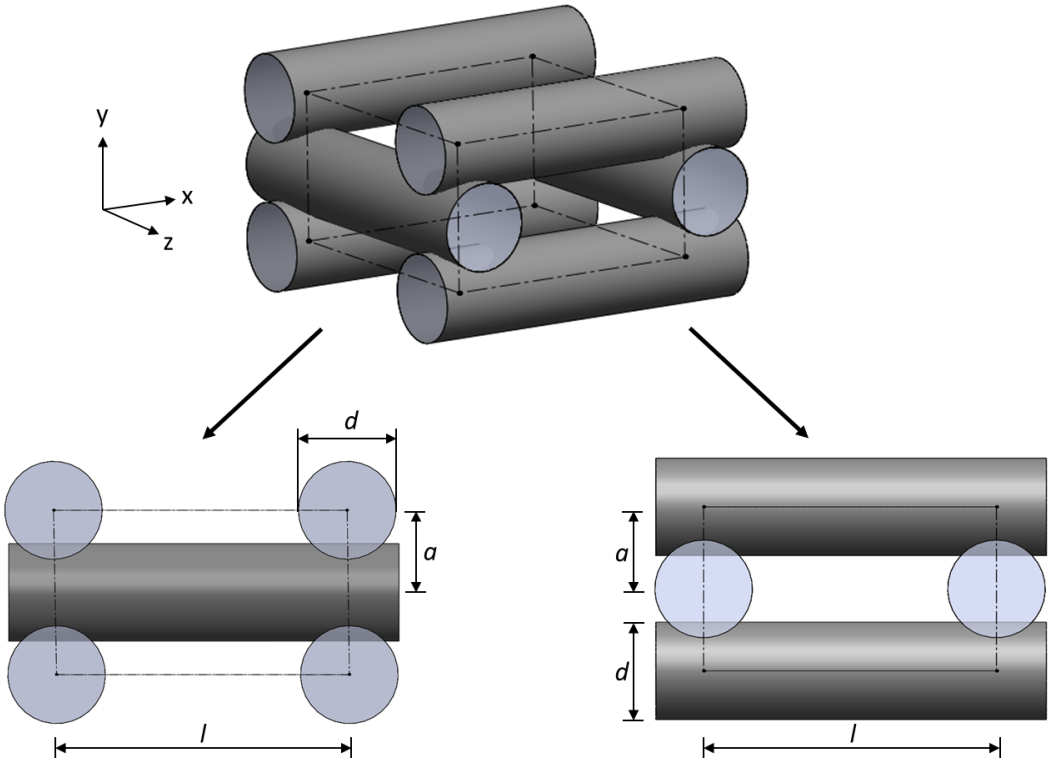

Figure 2-4: RVE of a 3D printed bone scaffold

we assume a more practical range of $d/l \in [0.3, 0.8]$.[3]

As mentioned at the beginning of this chapter, we assume this bone scaffold will be used on flat bones, or flat sections of irregular bones (such as in the mandible). This simplifies the cellular solids model development by only requiring in-plane elastic constants. These bones are innately thin in relation to the overall bone dimensions, thus we assume they are in plane stress. Due to the symmetry of the scaffold, we can expect it to be orthotropic. Due to the symmetry and planarity, we only need obtain expressions for three independent elastic constants, namely the longitudinal modulus $E_{11}^* = E_{22}^*$, the shear modulus G^*, and the Poisson's ratio ν^*.

2.4.3 In-Plane Longitudinal Modulus

Norato and Wagoner Johnson previously calculated the in-plane longitudinal modulus [28]. Deformation in the RVE is caused by uniaxial extension of the rods, which additionally experiences a plane strain effect caused by the adjacent layers. Following the cellular solids method, we apply a far-field stress σ_x in the x direction and find the equivalent load on the rods (cf. figure 2-4) as

$$P = 2\sigma_x a l \tag{2.22}$$

[3] A more detailed rationale for the lower bound is detailed in section 2.4.4

The presumed RVE deformation is captured by

$$\epsilon_x = \underbrace{\epsilon_x^u}_{\text{uniaxial extension}} + \underbrace{\epsilon_x^{ps}}_{\text{plane strain effect}} \tag{2.23}$$

where

$$\epsilon_x^u = \frac{\sigma_x}{E_s} \tag{2.24}$$

If no plane strain effect were present, the deformation in the y-axis would be

$$\epsilon_y^u = -\nu_s \epsilon_x^u \tag{2.25}$$

In the presence of plane strain, necessarily ϵ_y^u should be zero, which means the above deformation must be balanced by a deformation

$$\epsilon_y^{ps} = -\epsilon_y^u = \nu_s \epsilon_x^u \tag{2.26}$$

Therefore,

$$\epsilon_x^{ps} = -\nu_s \epsilon_y^{ps} = -\nu_s^2 \epsilon_x^u \tag{2.27}$$

In the above, ν_s is the Poisson's ratio of the bulk material. Substituting equation (2.27) into (2.23) gives

$$\epsilon_x = (1 - \nu_s^2)\epsilon_x^u \tag{2.28}$$

Thus $(1 - \nu_s^2)$, as is known in mechanics, is the plane-strain modifying factor. The rod deformation is given by

$$\epsilon_x = \frac{P}{AE_s} \tag{2.29}$$

where A is the cross-sectional area of the rod. Substituting equation (2.28) into equation (2.29), and with $A = \pi d^2/4$ we have

$$\epsilon_x = \frac{8\sigma_x a l (1 - \nu_s^2)}{\pi d^2 E_s} \tag{2.30}$$

We note that the effective scaffold deformation is equal to

$$\epsilon_x^s = \frac{\sigma_x}{E_{xx}^*} \tag{2.31}$$

Equating equations (2.30) and (2.31) and rearranging gives

$$\boxed{\frac{E_{xx}^*}{E_s} = \frac{C_1 \pi}{8(1-\alpha)(1-\nu_s^2)} \left(\frac{d}{l}\right)} \tag{2.32}$$

This is the uncalibrated cellular solids model, which is formulated in terms of d/l. E_{zz}^*/E_s is equivalent due to symmetry as aforementioned.

2.4.4 Shear Modulus

The RVE for the calculation of the effective shear modulus is the same as the one in figure 2-4. The far-field stress, as in the example of 2.2.3.6, is a shear stress τ_{xz}. Using finite element analyses, we determined that the RVE deformation was primarily given by bending of the transverse rods.

When the bone scaffold is sheared, the fully effective joints resist torsional deflection. This deflection is a function of the overlap ratio α. As the rods intersect less (i.e. smaller α) this torsional resistance decreases. To simulate the joints' torsional resistance, we consider one end of the rod to be entirely fixed, while the other end is free to translate but has zero rotation, as depicted in figure 2-5 [37]. From this figure, it is clear that a moment is imparted

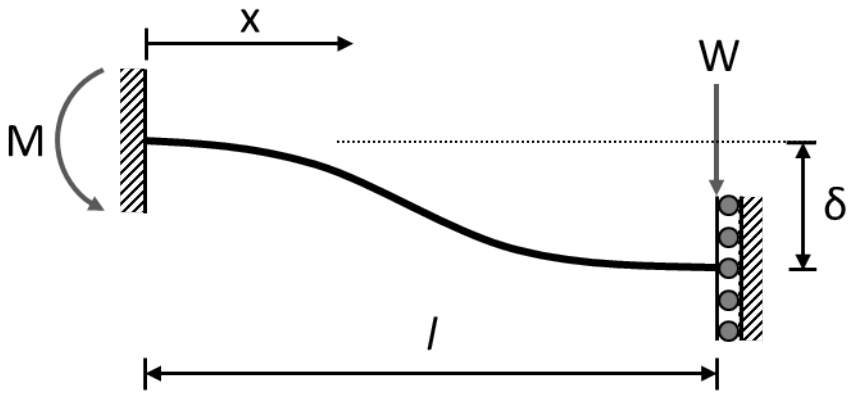

Figure 2-5: Beam bending of an RVE rod (adapted from [37])

at both ends so that the slope is zero at these locations. The slider allows vertical deflection but no horizontal deflection, although the beam has no axial deformation in Euler-Bernoulli beam theory. From [37], the deflection of a beam with these boundary conditions is

$$\delta = \frac{Wx^2}{12E_sI}(3l - 2x) \tag{2.33}$$

where $I = \pi d^4/16$ for a circular cross-section with diameter d. The maximum deflection occurs when $x = l$ resulting in

$$\delta_{max} = \frac{Wl^3}{12E_sI} \tag{2.34}$$

The equivalent load, determined based on figure 2-4, is given by

$$W = 2\tau al \tag{2.35}$$

The macroscopic deflection of the scaffold from Hooke's law is

$$\gamma = \frac{2\tau}{G^*} \tag{2.36}$$

where G^* is the effective shear modulus of the scaffold. As in example 2.2.3.6, we have that

$$\gamma = \frac{\delta}{l} \tag{2.37}$$

Substituting this equation into equation (2.34) yields

$$\gamma = \frac{Wl^2}{12E_sI} \tag{2.38}$$

By equating the deformations of the RVE and the scaffold and rearranging, we find

$$\begin{aligned} G^* &= \frac{12E_sI}{al^3} \\ &= \frac{3G_s(1+\nu_s)(\pi d^4)}{8al^3} \end{aligned} \tag{2.39}$$

where we used the fact that $E_s = 2G_s(1+\nu_s)$ from Hooke's law. Up to this point, the joint is assumed to be fully rigid in rotation; however, as the rod overlap ratio α decreases, the reaction moment imparted by the joints on the embedded rods reduces and allows further deflection. To reflect this, we thus scale by α the effective shear modulus, leading to

$$\boxed{\frac{G^*}{G_s} = C_2\alpha\frac{(1+\nu_s)}{(1-\alpha)}\left(\frac{d}{l}\right)^3} \tag{2.40}$$

where we introduced the unknown coefficient C_2 and used equation (2.21). This is the cellular solids model for the bone scaffold shear modulus based solely on a rod bending deformation assumption. When calibrated to the data, there is a poor data fit for low d/l. By observing the FE analysis, we found there is another deformation mode contributing to the effective shear modulus for scaffolds with low d/l. In this scenario, there is a greater torsion applied to the joints due to a larger spar length and the rod of figure 2-5 will not bend but primarily stretch as its length increases. This is equivalent to having hinges at the joints. The regression analysis of section 2.5.2 finds that this effect is negligible, particularly at higher d/l values greater than 0.3. Additionally, to avoid unstable structures, we wish to design a scaffold with a d/l greater than 0.3, hence we omit the rods' axial deformation in the effective shear modulus model.

2.4.5 Poisson's Ratio

The Poisson's ratio RVE deformation assumes a transverse contraction along the rods as the scaffold is stretched longitudinally. This is typical of any solid material, where $\epsilon_{11} = -\nu\epsilon_{22}$; however, in this case, the transverse contraction of the scaffold is only due to the contraction of the sinter joints. When a rod is stretched, it contracts radially. This radial strain is passed to the transverse rods through the sinter joint. More sinter joints per unit are thus dictate a larger Poisson's ratio. Intuitively, a larger overlap ratio α induces more radial rod contraction in the transverse rod. We therefore assume the effective Poisson's ratio to be

proportional to α and d/l.

To find the rod contraction transferred to the transverse rod, we find the average deformation along the x axis seen in figure 2-6. We place a unit strain along the z-axis, normal

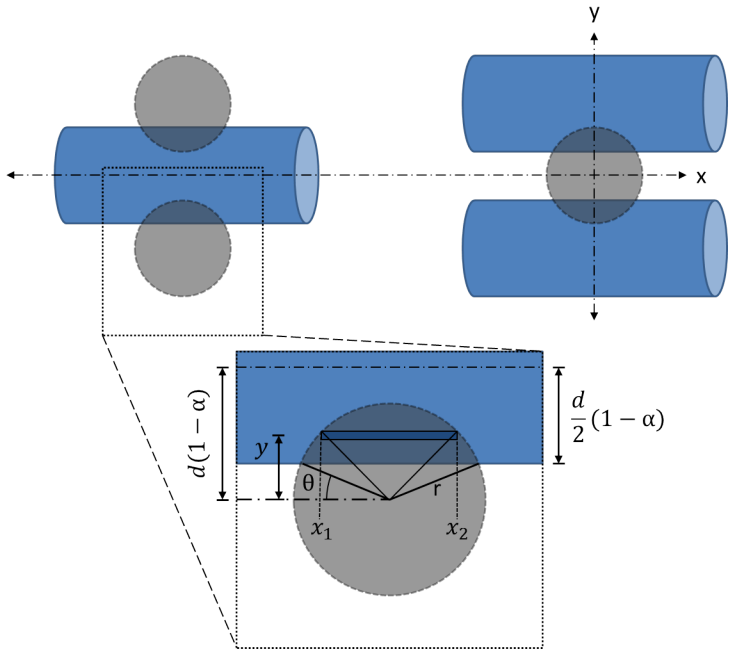

Figure 2-6: Poisson's ratio effect within the RVE

to the detail view of figure 2-6. The bone scaffold deformation is defined as

$$\epsilon_x = -\nu^* \epsilon_z \tag{2.41}$$

We know ν_s and ϵ_z. We need to formulate the ϵ_x deflection model to relate the RVE geometry to the macroscopic Poisson's ratio of the scaffold. In the detail view of figure 2-6, the proportional deformation for the infinitesimally small slice shown is

$$\int_{x_1}^{x_2} \frac{\nu_s}{l} dx \tag{2.42}$$

where $x_1 = -r\cos(\theta)$ and $x_2 = r\cos(\theta)$. θ is the angle from the horizontal to where the rod intersects the slice (see figure 2-6). Then the average x-deformation of the entire intersection due to a strain in the z-direction is

$$\epsilon_{\bar{x}} = \frac{2\epsilon_z}{dl} \int_{\frac{d}{2}(1-\alpha)}^{\frac{d}{2}} \int_{-\frac{d}{2}\cos(\theta)}^{\frac{d}{2}\cos(\theta)} \nu_s \, dx \, dy \tag{2.43}$$

From the geometry, we find that

$$\begin{aligned} \sin(\theta) &= \frac{d}{2}(1-\alpha)\frac{1}{d/2} = 1-\alpha \\ \theta &= \arcsin(1-\alpha) \end{aligned} \tag{2.44}$$

We use the identity, $\cos^2(\theta) + \sin^2(\theta) = 1$ to relate the geometry from equation (2.44) to the bounds in equation (2.43) to obtain

$$\cos(\theta) = \sqrt{2\alpha(1-\alpha)} \tag{2.45}$$

Now we can update the bounds in equation (2.43) by substitution of $\cos(\theta)$ and solve for ν^*.

$$\epsilon_{\bar{x}} = \frac{2\epsilon_z}{dl} \int_{\frac{d}{2}(1-\alpha)}^{\frac{d}{2}} \int_{-\frac{d}{2}\sqrt{2\alpha(1-\alpha)}}^{\frac{d}{2}\sqrt{2\alpha(1-\alpha)}} \nu_s \; dx \; dy \tag{2.46}$$

After evaluating the integral, rearranging and introducing a constant, and by using equation (2.41), we obtain

$$\boxed{\frac{\nu^*}{\nu_s} = C_3 \alpha \sqrt{2\alpha(1-\alpha)} \left(\frac{d}{l}\right)} \tag{2.47}$$

This corroborates our deformation assumptions, and it indicates that the effective Poisson's ratio is proportional to the relative density. We now have equations for the bone scaffold's longitudinal moduli, shear modulus and Poisson's ratio. The following section details the procedure to determine numeric values for the constants C_1, C_2, and C_3 in equations (2.32), (2.40), and (2.47) respectively.

2.5 Numerical Calibration of the Bone Scaffold

2.5.1 Computational Design of Experiments

The constants C_1, C_2, and C_3 in equations (2.32), (2.40), and (2.47) are to be determined by regression to a set of numerical experiments. As discussed in section 2.3.3, a computational design of experiments is employed to capture the effect of all parameters. The following factors and their levels are presented in table 2.1.

Factor	**Levels**
α	[0.05 0.10 0.15 0.20 0.25 0.30 0.35 0.40 0.45]
d/l	[0.10 0.20 0.30 0.40 0.50 0.60 0.70 0.80]
ν	[0.2 0.225 0.25 0.275 0.3 0.325 0.35]

Table 2.1: Factors and their levels used in the computational design of experiments

A full factorial design results in $9 \times 8 \times 7 = 504$ experiments. As discussed earlier, six finite element analyses are performed for each of these experiments, and the results of the six analyses are input into either equation (2.16) or (2.17). The result is 504 effective stiffness tensors. The geometry specification and meshing for these numerical experiments are very difficult to robustly automate if the mesh in the RVE is to conform to the geometry of the scaffold. To alleviate this difficulty, we employ the geometry projection method [28, 38], whereby the geometry of any scaffold RVE is projected onto a fixed uniform grid

for automated analysis. The projection of the geometry onto the analysis grid is effected by modifying the material properties, i.e. by using the so-called ersatz material. This method provides for an efficient and robust way of automatically generating and analyzing all the designs in the sample. In this section, we describe the geometry projection scheme and its computer implementation using the open source finite element library deal.II [39]. We validate the geometry projection by comparison to numerical homogenization results obtained using Python scripting and the commercial finite element code ABAQUS on a few RVE geometries, whereby we employ grids that conform to the scaffold geometry. Finally, we describe the automation of the execution of the design of experiments.

2.5.1.1 Geometry Projection

To circumvent the geometry creation and re-meshing issue, we use the geometry projection method [38]. The scaffold RVE, described by the geometric parameters d/l and α, is projected onto a uniform grid of uniform hexahedral elements. The geometry projection assigns a 'density' to each element in the grid, which ranges between 0.0 and 1.0. This density is not a material property, but it signifies an allocation of material. A density of 1.0 indicates an element is fully occupied by material, whereas a density of 0.0 indicates the element is void of material [28, 32]. Intermediate density regions, by extension, indicate the element is partially occupied by material. Figure 2-7 shows an example of the geometry projection of a rectangular bar. Elements that fall entirely outside the bar have a density of 0.0 (i.e. those

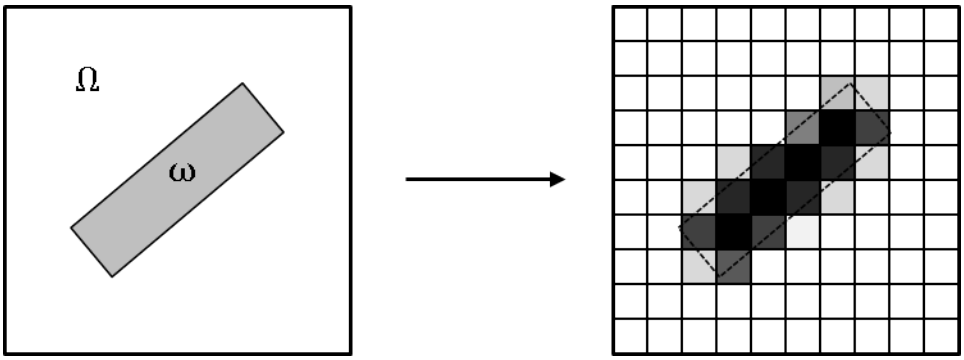

Figure 2-7: Geometry projection representation (right) of a bar ω upon a fictitious domain Ω (left)

that appear white in the figure); those that fall entirely inside have a density of 1.0 (i.e. those that appear black); and elements that only partially intersect the bar have an intermediate density (i.e. the gray region along the bar's boundary). The geometry projection is reflected in the analysis by weighting the material elasticity tensor in the element by the density, i.e.

$$\mathbf{E}_e = \rho_e \mathbf{E}_s \tag{2.48}$$

where $\mathbf{E}_e$ is the weighted elasticity tensor, and ρ_e the density for element e, and $\mathbf{E}_s$ is the bulk material elasticity tensor. Here, the density is defined as the intersection volume of the sphere that circumscribes the element with the scaffold geometry, divided by the volume of

the sphere, i.e

$$\rho_e := \frac{|\mathbf{B}_e \cap \omega|}{|\mathbf{B}_e|} \tag{2.49}$$

where $\mathbf{B}_e$ denotes the ball centered at the centroid of element e and that circumscribes the element, ω denotes the domain occupied by the scaffold, and $|\cdot|$ is the measure (i.e. volume). In general, the exact shape of the intersection volume $\mathbf{B}_e \cap \omega$ is unknown and can have a

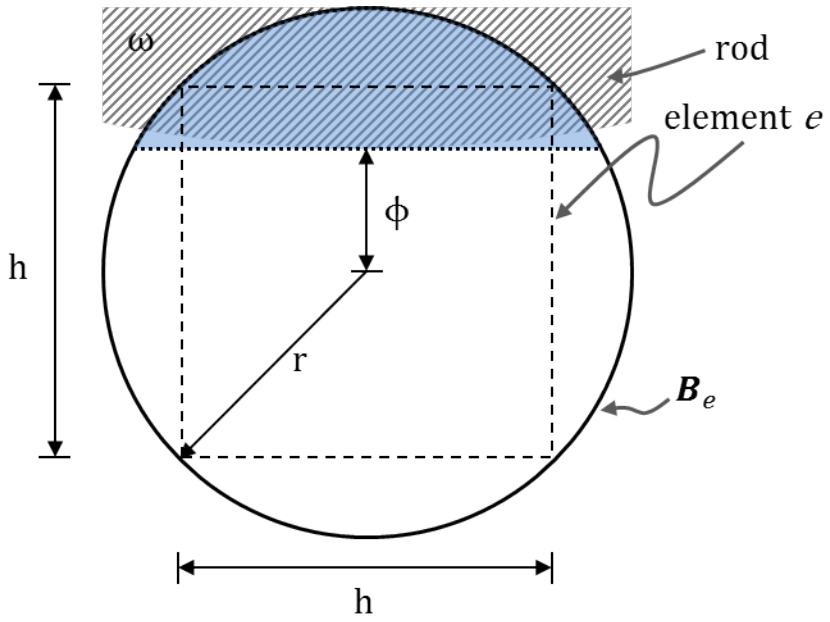

Figure 2-8: The sampling window for a finite element used to compute the element density in the geometry projection

complex shape. However, if we assume that $\mathbf{B}_e$ is very small in comparison to ω, we can approximate the intersection volume as the spherical cap whose circular base lies at the shortest signed distance ϕ from the element centroid (see figure 2-8). With that simplification, ρ_e can be readily computed as a function of the signed distance ϕ as

$$\rho_e(\phi) = \begin{cases} 0 & \text{if } \phi > r \\ \frac{(\phi - r)^2(\phi + 2r)}{4r^3} & \text{if } -r \leq \phi \leq r \\ 1 & \text{if } \phi < r \end{cases} \tag{2.50}$$

where ϕ is the distance from the element centroid to the scaffold geometry, h is the element size, and $r = \sqrt{2}h$ is the sampling sphere radius. In the analysis, elements with zero densities will make the problem ill-posed (i.e. it has infinite solutions); numerically, the zero densities will lead to zero diagonal elements in the assembled global stiffness matrix, which will cause the linear solution to fail. To circumvent this, we introduce a small lower bound on the density:

$$\tilde{\rho}_e := \rho_{min} + (1 - \rho_{min})\rho_e \tag{2.51}$$

Typically, a value of $\rho_{min} = 0.001$ is used. Accordingly, the element elasticity tensor is modified as

$$\mathbf{E}_e = \tilde{\rho}_e \mathbf{E}_s \tag{2.52}$$

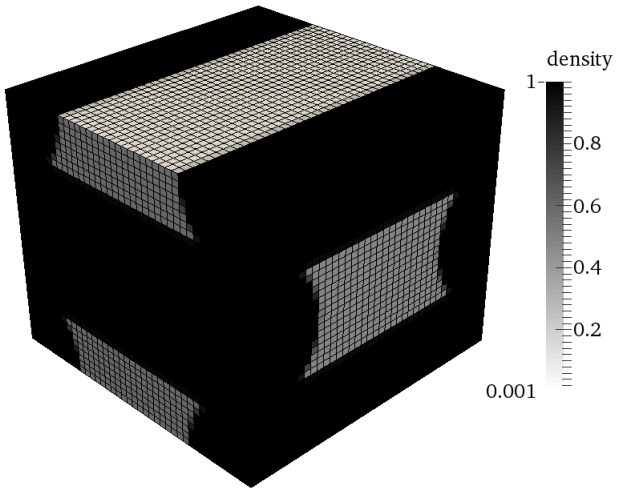

Figure 2-9: Projected geometry of bone scaffold RVE

With this modified elasticity tensor, the homogenized tensor of equation (2.16) is now given as

$$\mathbf{E}^H = \frac{1}{|V|} \sum_e \tilde{\rho}_e \int_{v_e} \left(\mathbf{I} - \mathbf{B}_e \boldsymbol{\chi}_e\right)^T \mathbf{E}_s \left(\mathbf{I} - \mathbf{B}_e \boldsymbol{\chi}_e\right) dv \tag{2.53}$$

whereas equation (2.15) is modified to

$$\begin{aligned} \mathbf{f}^{kl} &= \sum_e \tilde{\rho}_e \int_{v_e} \mathbf{B}_e^T \mathbf{E}_s \epsilon^{0(kl)} dv \\ \mathbf{K} &= \sum_e \tilde{\rho}_e \int_{v_e} \mathbf{B}_e^T \mathbf{E}_s \mathbf{B}_e \, dv \end{aligned} \tag{2.54}$$

Accurate solutions can be attained with this method provided that the element size remains much smaller than the minimum feature size of the bone scaffold. The geometry projection of an RVE with $d/l = 0.5$ and $\alpha = 0.15$ onto a $40 \times 40 \times 40$ elements mesh is shown in figure 2-9. Note that the areas of high density (shown in black) resemble that of the ideal RVE in figure 2-4.

2.5.1.2 Computer Implementation

The periodic boundary conditions (PBCs) are imposed by tying the degrees of freedom of pairs of nodes in opposing faces using the library utilities. An exhaustive search finds all element free faces and assigns them an ID (from one to six) corresponding to an RVE face. Using this ID, a built-in deal.II function then automatically creates the constraints, which are then applied to the sparse global stiffness matrix. These PBCs are sufficient to eliminate rigid body rotations, but not translations. Weak ground springs are therefore connected to all corner nodes of the RVE to eliminate all rigid body motion.

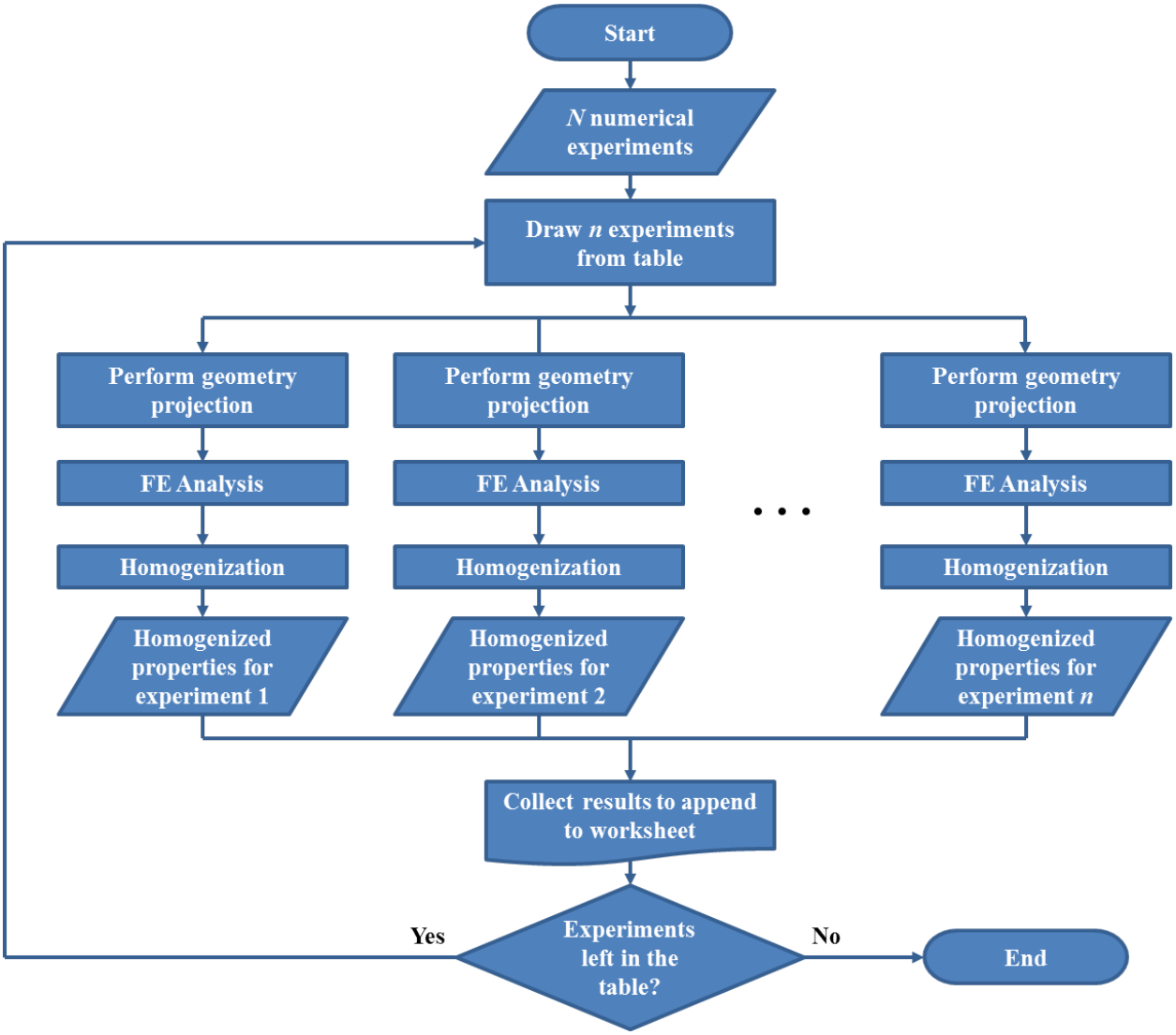

Figure 2-10: Flow chart to perform automated homogenization of all RVEs of table 2.1 using MPI for Python

The global stiffness matrix $\mathbf{K}$ of equation (2.54) is calculated once per numerical experiment along with the applied body loads resulting from each of the six unit test strains $\epsilon^{0(kl)}$. We then run the corresponding finite element analyses for these six loads and store the

resulting displacements. The strains resulting from these displacements are subsequently computed at each element quadrature point using library functions and used in equation (2.53) to obtain the homogenized elasticity tensor.

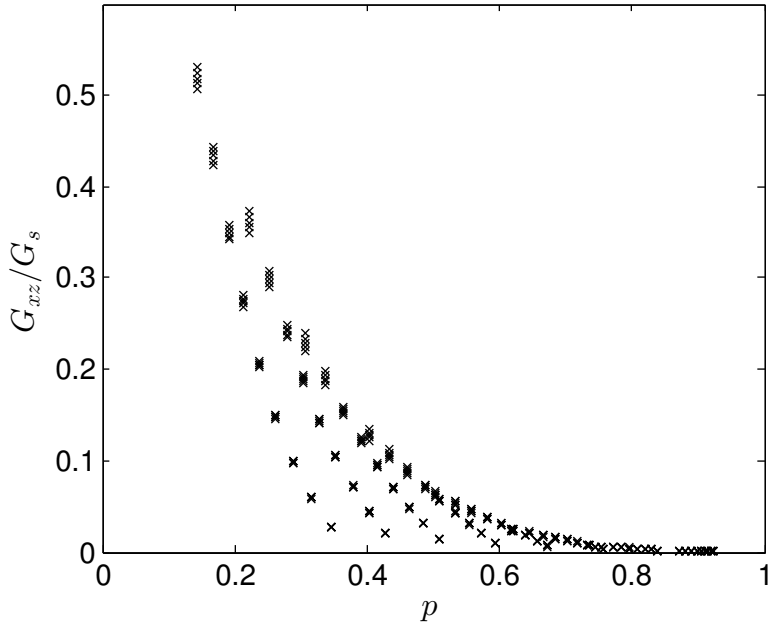

Figure 2-11: Result of the 504 computational design of experiments, showing the entire numerical data set for G_{xz}/G_s versus porosity

A Python script was written to automate the entire process, as depicted in figure 2-10. Since the analyses for all numerical experiments are independent, we can make use of a high performance computing (HPC) system to perform several experiments simultaneously — as many as compute nodes. To this end, we employ MPI for Python to distribute the compute jobs [40]. The script draws as many combinations from table 2.1 as compute nodes are available, performs the analyses, and writes the resulting homogenized properties to a Microsoft Excel spread sheet. The result of this computational design of experiments for the relative effective shear modulus is presented in figure 2-11.

2.5.1.3 Validation

To ensure the numerical homogenization scheme using the geometry projection is accurate, we compare the effective properties to those obtained with a conforming mesh for a few RVEs using ABAQUS. In addition, we compare the porosity obtained from the geometry projection to an analytical expression. The former is computed from

$$p = 1 - \frac{1}{|V|} \int_{\Omega} \tilde{\rho}_e dv \tag{2.55}$$

whereas the latter is given by [28]

$$p = 1 - \frac{1}{1-\alpha}\left[\frac{\pi}{4}\left(\frac{d}{l}\right) - \frac{2\big(1 - g(\epsilon = 1-\alpha)\big)}{3}\left(\frac{d}{l}\right)^2\right] \tag{2.56}$$

where

$$g(\epsilon) = 1 + 2\epsilon^2 F\left(\frac{\pi}{2}, 1-\epsilon^2\right) - (1+\epsilon^2)E\left(\frac{\pi}{2}, 1-\epsilon^2\right) \tag{2.57}$$

with F and E respectively denoting the first and second kind complete elliptic integrals.

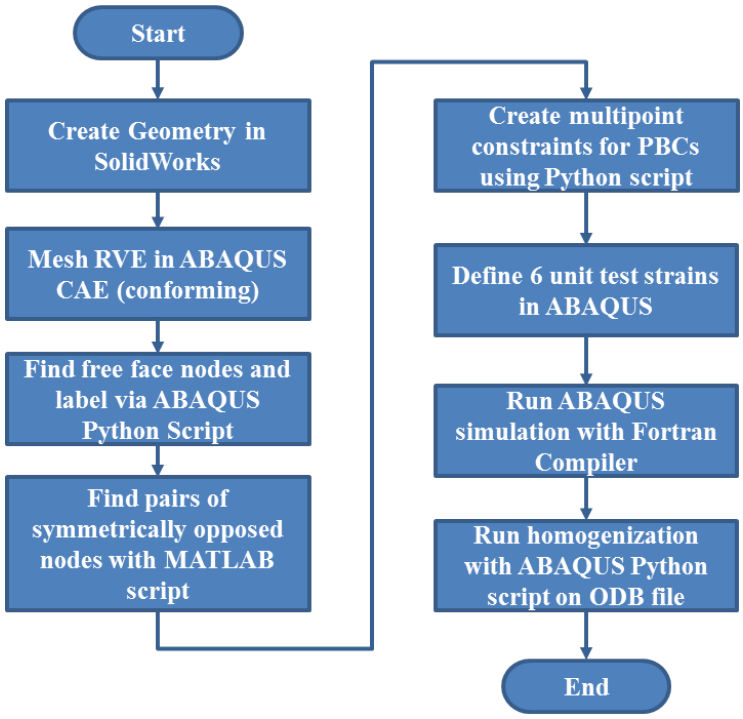

Figure 2-12: Flow chart to perform homogenization of an RVE using ABAQUS

The method to perform homogenization for a scaffold geometry using ABAQUS is outlined in figure 2-12. As depicted in the flowchart, a geometry associated with table 2.1 is created in SolidWorks 2014 and imported into ABAQUS CAE with the ACIS 3D Modeler file format. Subsequently, 20-node hexahedral quadratic interpolation continuum elements with reduced integration (C3D20R) and 10-node tetrahedral quadratic interpolation continuum elements (C3D10) are used to mesh the scaffold RVE as exemplified in figure 2-13. The main deflection mode of the rods is bending and when the rods are slender, spurious shear locking or hour-glassing modes arise when using linear interpolation (or constant strain) elements, which motivates our choice of quadratic interpolation elements.

Next, the periodic boundary conditions are imposed using an ABAQUS Python script that interfaces with the ABAQUS input model file (of extension .cae). Periodic boundary conditions can be imposed using either tie constraints with a prescribed distance between surfaces (using the *TIE ABAQUS Keyword) [34] or linear multipoint constraints (using the *EQUATION Keyword) [41]. We opt for the latter, which are more readily automated via

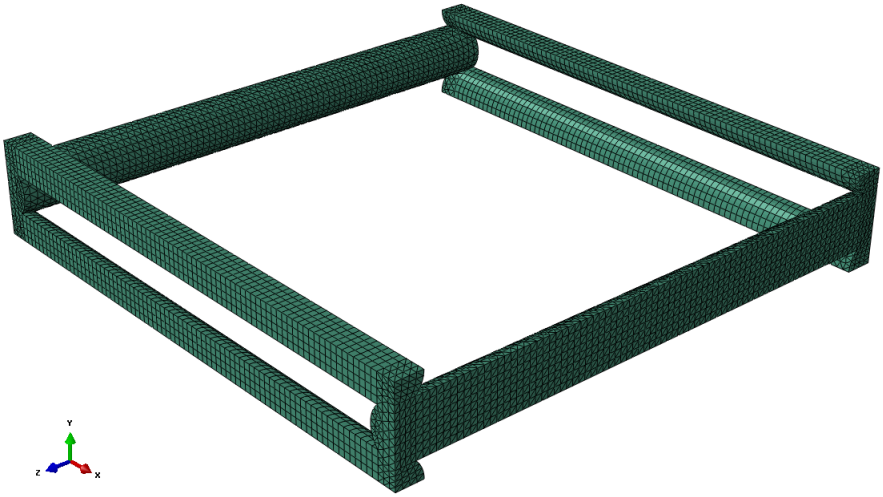

Figure 2-13: ABAQUS mesh representing a bone scaffold RVE of $\alpha = .15$ and $d/l = .1$

scripting. Multipoint constraints are defined as a linear combination of nodal displacements that add to zero (homogeneous equation) or to an admissible displacement (nonhomogeneous)

$$A_1 u_i^l + A_2 u_j^m + \cdots + A_N u_k^n = \delta \tag{2.58}$$

where A are the specified coefficients, u are displacements with subscripts referring to degree of freedom and superscripts referring to node number, and δ is a specified constant [41]. The choice of A and δ depends on the kind of constraint we want to impose. In the case of PBCs, specifically, a pair of nodes m and n symmetrically opposed with respect to the RVE mid Y-Z plane would be constrained as

$$\begin{aligned} u_1^m - u_1^n &= 0 \\ u_2^m - u_2^n &= 0 \\ u_3^m - u_3^n &= 0 \end{aligned} \tag{2.59}$$

that is, $A_1 = 1$, $A_2 = -1$, $\delta = 0$. A Python script (adapted from [41]) first finds all nodes on element free faces, and labels them with the RVE face ID on which they lie. Then, a MATLAB script compares the locations of all nodes in two opposing RVE faces and pairs each node with its closest mate using the statistics toolbox function *pdist2*. The paired nodes list is sent back to the Python script, which then writes multipoint constraints for each node pair. Special care must be taken to remove duplicate equations for corner and edge nodes, which would cause ABAQUS to fail to update the stiffness matrix due to missing information. Once all unique multipoint equations are applied, all faces of the RVE will be accounted for as shown in figure 2-14. All yellow dots are nodes within a multipoint constraint equation.

To apply the six unit test strains in ABAQUS, we employ thermal strains defined as [34]

$$\epsilon^{0(mn)} = \kappa^{mn} \Delta T \tag{2.60}$$

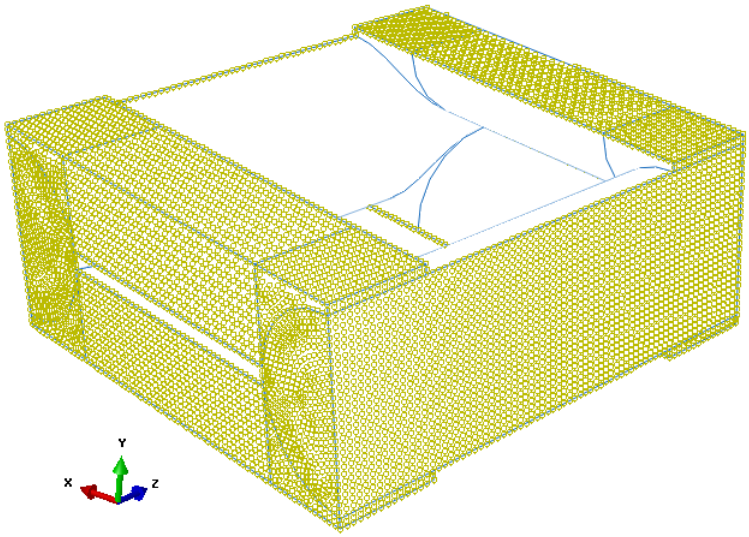

Figure 2-14: RVE in ABAQUS showing all multipoint constraint equations

where $\Delta T = 1$ and κ is a thermal expansion coefficients 2-tensor defined as

$$\kappa_{ij}^{mn} = \kappa_{ji}^{mn} = \begin{cases} 1 & \text{if } i = m \text{ and } j = n \\ 0 & \text{otherwise} \end{cases} \tag{2.61}$$

When applied in ABAQUS, we employ the Voigt vector representation of the strain and of κ. Six linear perturbation steps are defined in ABAQUS where in each step we apply one of the test unit strains of equation (2.60). Using the ABAQUS user-defined subroutine UEXPAN, we manually define the temperature-dependent thermal strain, i.e., we link each unit strain to its perturbation step with its corresponding temperature. With this implementation, each step in the finite element solution has no impact on subsequent steps, and we obtain the six different finite element solutions necessary for homogenization [34] as seen in figure 2-15. To perform the ABAQUS analyses, we use the Intel Fortran Compiler 12 to compile the user-defined subroutine.

The last step, as shown in figure 2-12 is to use a Python script to open the output database (.ODB) file, read all resulting stresses for each loading step, and solve for the effective elasticity tensor via equation (2.17).

The process of figure 2-12 is performed only for three scaffold geometries due to the laborious, manual effort required to create each scaffold design solid model and finite element mesh. A comparison of the in-plane homogenized properties is shown in table 2.2. As can be seen in the table, there is a good level of agreement between the ABAQUS and deal.II numerical homogenization procedures for the tested geometries, particularly for the moduli. The error in the Poisson's ratio for the second geometry, with $\alpha = 0.2$ and $d/l = 0.1$ is large, while it is small for the other geometries. This discrepancy can be attributed to numerical error primarily caused by the geometry projection. The geometry projection error (i.e. the error related with how well the projected density captures geometric features) is exacerbated for low d/l, since the rods are very slender and their diameter very small in comparison to

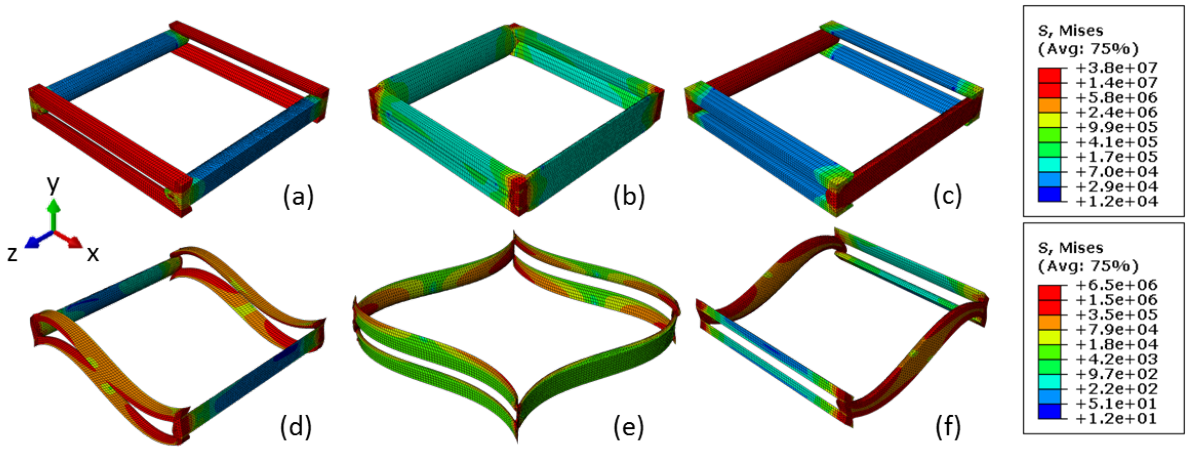

Figure 2-15: Von Mises contour plot of an RVE with $\alpha = 0.15$ and $d/l = 0.1$ for applied test strains: (a) $\epsilon_{11} = 1$; (b) $\epsilon_{22} = 1$; (c) $\epsilon_{33} = 1$; (d) $\epsilon_{12} = 1$; (e) $\epsilon_{13} = 1$; and (f) $\epsilon_{23} = 1$.

the dimensions of the RVE, which means that features such as the overlap between rods are not accurately resolved in the projection. In practice, however, we are not interested in low d/l scaffolds since the resulting stiffness is insufficient for load bearing, and they would easily buckle under compressive load. Since we are not after highly accurate predictions of the effective properties, but instead we look for a degree of accuracy suitable for efficient execution of the computational design of experiments, we do not perform more extensive validation (for instance, by examining the effect of mesh refinement), and we are content with the level of accuracy observed for these three tests.

As another validation check, we compared the porosity obtained via the geometry projection, using equation (2.55), to an analytical expression of the porosity, using equations (2.56) and (2.57). The comparison is plotted in figure 2-16. The lines represent the analytical porosities whereas the points are porosities calculated using the geometry projection. The maximum error is 0.011, proving the accuracy of the geometry projection [28].

2.5.2 Least Squares Nonlinear Regression

Using the geometry projection-based numerical homogenization, we perform the computational design of experiments and we obtain effective in-plane properties for all of the scaffold design combinations of table 2.1. With this data set, we can now calibrate the cellular solids models using the least squares regression of equation (2.19), where the properties obtained from the numerical homogenization experiments correspond to the $ydata_i$. MATLAB R2014a was used to perform the nonlinear least squares regression on the C_i scalar coefficients.

The calibrated cellular solids model of the shear modulus is plotted against the discrete numerical homogenization points in figure 2-17. The calibrated constant is $C_2 = 1.011$ of equation (2.40). The regression error infinity norm is 0.0161, which indicates that the calibrated cellular solids model successfully adheres to the numerical homogenization predictions. For comparison, a quintic polynomial as a function of α and d/l was fit to the numerical data set through the nonlinear least squares regression. The error infinity norm was 0.0315. Not only is the polynomial a poorer fit to the data, but it has six constants

Homogeneous Properties					
	E_{xx}/E_s	E_{zz}/E_s	G_{zx}/G_s	ν_{zx}/ν_s	ν_{xz}/ν_s
Geometry: $\alpha = .45$, $d/l = .4$					
ABAQUS	.309	.309	.0617	.349	.348
deal.II	.310	.310	.0629	.340	.340
Error	.00131	.00131	.00127	-.00884	-.00784
Rel. Error	.00424	.00424	.0206	-.0253	-.0225
Geometry: $\alpha = .2$, $d/l = .1$					
ABAQUS	.0496	.0496	.000421	.0249	.0249
deal.II	.0462	.0462	.000447	.0364	.0364
Error	-.00343	-.00343	.0000264	.0115	-.0115
Rel. Error	-.06921	-.0692	.0627	.465	-.465
Geometry: $\alpha = .3$, $d/l = .6$					
ABAQUS	.373	.371	.118	.286	.284
deal.II	.374	.374	.122	.301	.301
Error	.00120	.00319	.00459	.0149	.0169
Rel. Error	.00321	.00862	.0389	.0520	.0594

Table 2.2: Comparison of in-plane homogenized properties obtained with conforming meshes (ABAQUS) and with geometry projection (deal.II)

instead of only two.

The Poisson's ratio cellular solids regression also shows agreement with the numerical data with $C_3 = 8.894$ in equation (2.47). The error infinity norm is 0.0417. A quadratic homogeneous polynomial of the form $C_1\alpha^2 + C_2\alpha(d/l) + C_3(d/l)^2 + C_4\alpha\nu + C_5(d/l)\nu + C_6\nu^2$ yields an infinity norm of 0.0482 which is slightly worse of an approximation than the cellular solids model. This polynomial fitting requires six fitted coefficients instead of one.

The Poisson's ratio calibrated cellular solids model is shown in figure 2-18. As the rods separate to infinity, there will be fewer sinter joints to transmit the transverse deflection, so the Poisson's ratio will tend to zero. As α decreases, there is less sinter joint volume to transmit transverse deflection, hence the Poisson's ratio decreases.

The longitudinal moduli were calibrated as shown in figure 2-19, resulting in $C_1 = 1.009$ in equation (2.32). The error infinity norm is 0.0504. With good agreement, this completes the numerical calibration of the cellular solids models.

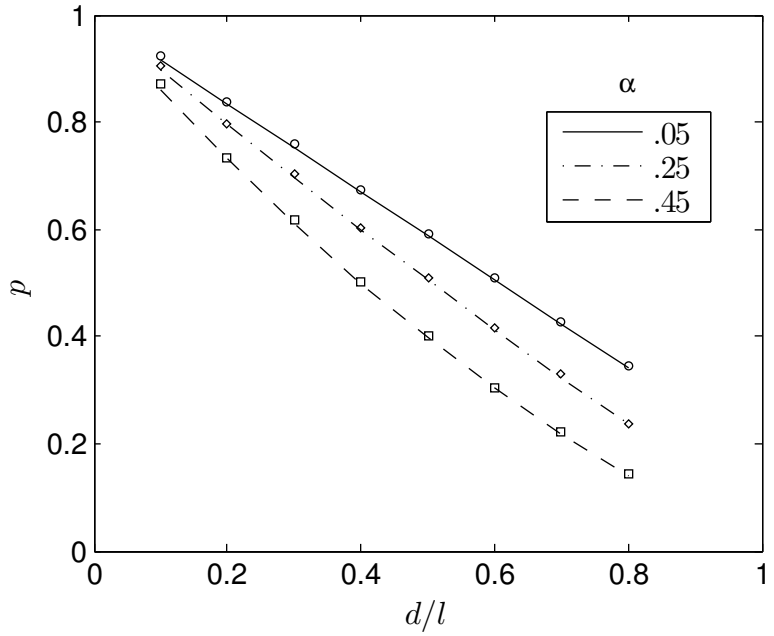

Figure 2-16: Analytical (lines) versus geometry projection (points) porosity as a function of d/l for different overlap ratios α.

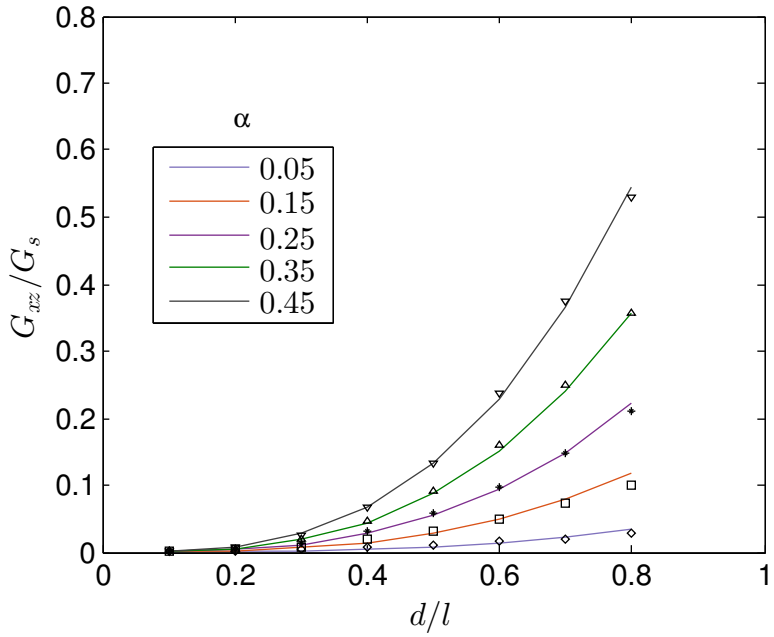

Figure 2-17: In-plane effective shear modulus versus d/l for $\nu = 0.3$ and various α overlap ratios

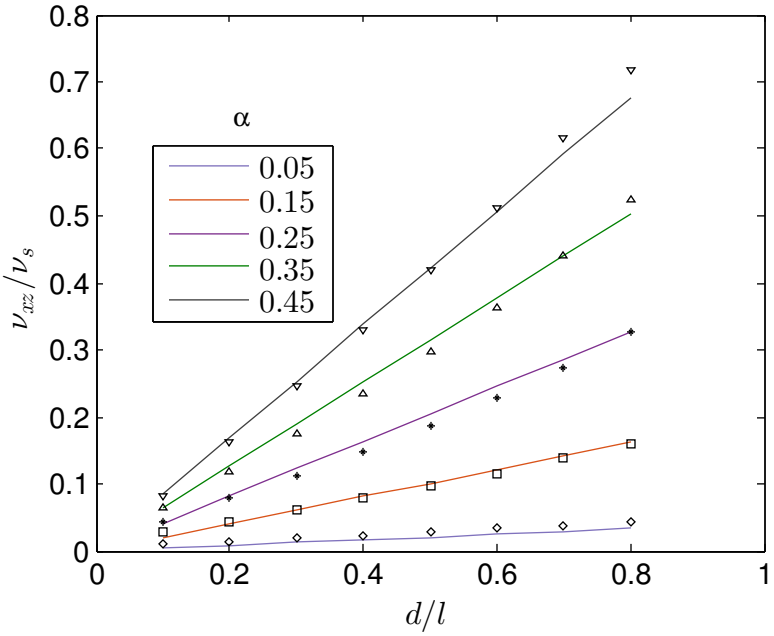

Figure 2-18: In-plane effective Poisson's ratio versus d/l for $\nu = 0.3$ and various α overlap ratios

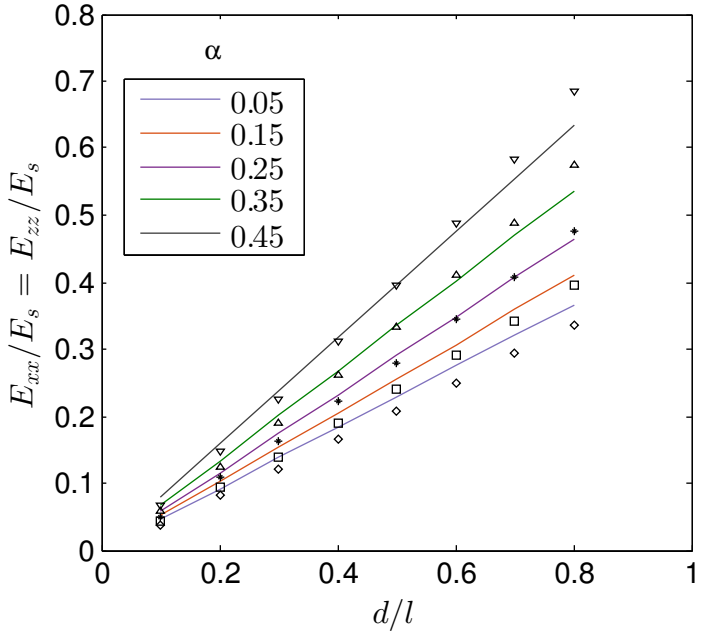

Figure 2-19: In-plane effective longitudinal modulus versus d/l for $\nu = 0.3$ and various α overlap ratios

Chapter 3

Scaffold Design

3.1 Design Requirements

The goal as discussed in the introduction is to create a bone scaffold that provides adequate support while having enough porosity to support bone in-growth. Existing research indicates that a minimum of 100-150 μm pore size is necessary for osteogenesis and ingrowth [10, 42]. The pore size must be large enough to allow capillary in-growth, and have a large enough surface area for osteointegration. A review of studies on biomaterial scaffold porosity for mandibles shows that to accommodate bone in-growth, typically porosities between 38 and 44% for mandibles are used [42].

To meet mechanical requirements, the stiffness needs to provide enough mechanical support to return function to the afflicted region, but it cannot be so high that it eliminates the load on the surrounding bone. If the defect is excessively load-bearing, the strain-related stimulus necessary to maintain bone falls below the minimum effective strain, and bone resorption ensues [43]. By tailoring the bone scaffold such that the stiffness is that of the native bone, the surrounding bone will undergo the mechanotransduction necessary to maintain bone mass and preclude bone tissue recession.

3.2 Existing Computational Scaffold Design Methodologies

Existing computational methods for scaffold design use different strategies and are geared towards different material systems than the one considered here. Dias et al. used density-based topology optimization to define optimal material distribution within a periodic RVE to attain a target stiffness while maximizing permeability. The material system they considered is selective laser sintering (SLS) of poly-ϵ-caprolactone-4%hydroxyapatite [44], cf. figure 3-1a.

Hollister et al. employ a 'restricted optimization' problem whereby homogenization theory is used to link the scaffold's unit cell micro-structural design parameters (i.e. voids defined by mutually orthogonal cylinders of diameters d_1, d_2, and d_3) to its effective stiffness tensor using a nonlinear least squares-fitted polynomial. The error between the stiffness tensors of the adapted bone and the scaffold with respect to specified targets is minimized subject to

a porosity constraint. They also maximize porosity subject to admissible ranges imposed on the adapted bone and scaffold stiffness tensors. An optimized periodic HA bone scaffold is generated using the target stiffness design by converting voxel data sets to an STL surface format for printing by a solid free form casting technique [45], cf. figure 3-1b.

Lin et al. built upon this approach and broadened the design space by employing density-based topology optimization utilizing numerical homogenization via finite elements. Again, the error between the homogenized effective and target stiffness tensors is minimized subject to a porosity constraint. The resulting scaffolds' stiffness tensors are found to be very close to samples taken from iliac crest and distal femur trabecular bones showing scaffold designs can match a multitude of material properties, although their porosities do not guarantee diffusivity. The scaffolds are printed using 3D Ink Jet Printing [46], cf. figure 3-1c.

To address the diffusivity issue, some, including Kang et al. have adopted diffusivity as part of the optimality criteria. Here, density-based topology optimization is utilized with numerical homogenization to find the effective diffusivity and elastic stiffness tensor of an RVE under PBCs. The error between both criteria and their targets is minimized in a multiobjective formulation subject to a volume constraint. The optimized structure exhibited an effective bulk modulus and diffusivity on the cross-property upper bounds, as anticipated. This method was applied to spinal fusion cages, resulting in a scaffold of high stiffness and high permeability to promote bone ingrowth for spinal fusion. The globally optimized scaffold had regions of solid, high density, and low density, with each section given specifically chosen microstructures to minimize compliance and maximize diffusivity [47], cf. figure 3-1d.

Sturm et al. also used density-based topology optimization, but used it to minimize the difference between a target material tensor and the homogenized effective properties of a periodic RVE. The target stiffness tensor is given as a fraction β of the host bone stiffness tensor. A bone remodeling simulation of the ensuing optimal topology is then performed to determine the bone growth volume after a specified time. The optimization-bone remodeling simulation is subsequently performed for different values of β to determine what fraction maximizes bone growth volume (which the authors find to be $\beta = 1$) [20], cf. figure 3-1e.

More recently, bone scaffolds were optimized by Boccaccio et al. to maximize bone ingrowth using a mechano-biology-based algorithm of parametric bone scaffolds with lattice-shaped porosity. The largest bone formation was found in scaffolds of high porosity and elliptic or rectangular cross-sections [48], cf. figure 3-1f.

Makowski and Kuś optimize bone scaffolds made via fused deposition modeling (FDM). Again, the error between a target stiffness and the scaffold's effective stiffness is minimized. The authors optimize square deposited rods' thicknesses and quantity in one RVE using an evolutionary algorithm. Rods in adjacent layers are left perpendicular to each other to facilitate the manufacturing process. The scaffold is manufactured as an assemblage of all RVEs cut to the shape of the defect [49], cf. figure 3-1g.

Lastly, Chen et al. utilize density-based topology optimization of a homogenized RVE to explore the effect of scaffold design on implant degradation and tissue ingrowth. The stiffness and permeability of the RVE are maximized subject to a volume fraction constraint in a weighted multi-objective biphasic topology optimization problem. A Pareto frontier is generated by changing the normalized weights of the competing objective functions (i.e., stiffness and permeability) and solving the optimization problem. Three exemplary RVEs

were chosen from the runs. Their polymer degradation and tissue ingrowth was studied numerically over a 70 day time period finding that increased permeability resulted in higher RVE stiffnesses after bone adaptation [19], cf. figure 3-1h.

We aim to contribute to this growing discipline by extending optimized bone scaffolds to non-periodic structures. We also simplify the approach by choosing an 'offline' optimization approach whereby we employ the cellular solids method. Lastly, we tailor our design specifically to direct ink writing and propose a novel technique to convert a finite element representation of an optimized scaffold to a manufacturable design.

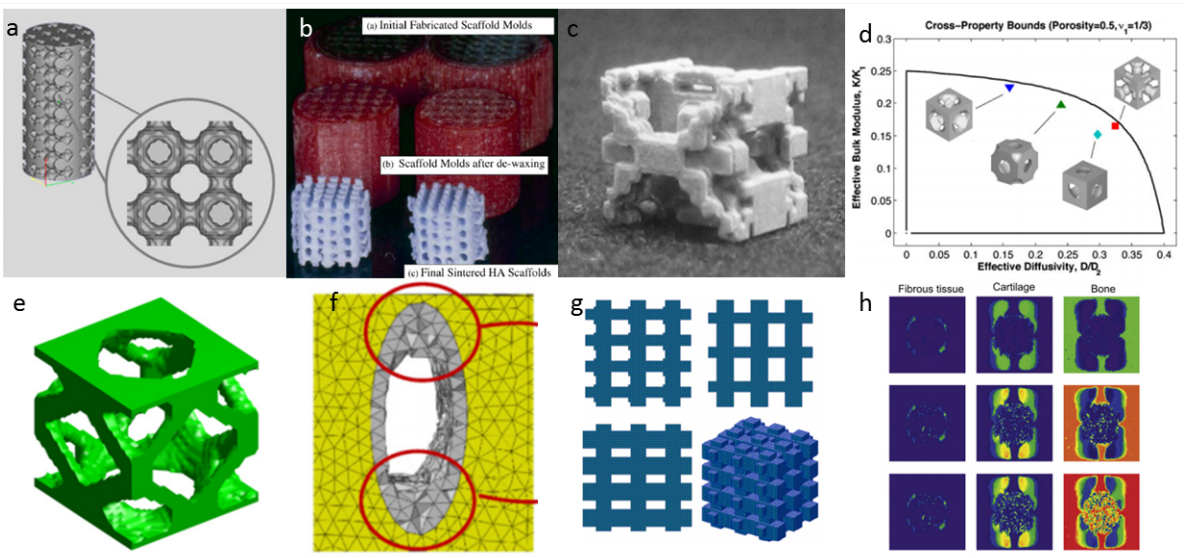

Figure 3-1: (a) [44]; (b) [45]; (c) [46]; (d) [47]; (e) [20]; (f) [48]; (g) [49]; (h) [19].

3.3 Proposed Design Method

In this work, we aim to design scaffolds made by direct ink writing whose geometric configuration is shown in figure 1-2. To conform to the manufacturing process, and in accordance with our cellular solids models, we employ as design variables those geometric parameters that can be controlled in the fabrication. These are d/l, which can be controlled by the choice of nozzle diameter and by the deposition path, and the orientation ψ of the tangent vector to the rod axis, which determines the rod curvature and which can also be controlled by the deposition path. On the other hand, the direct ink writing process offers little control of the overlap α, and the solid material Poisson's ratio is fixed. Therefore, we keep these parameters constant.

The optimization thus occurs on the effective orthotropic elasticity tensor. From equations (2.32), (2.40), and (2.47) we have all of the elasticity constants that we need to assemble the effective elasticity tensor for the bone scaffold. With a plane stress assumption, the entire elasticity tensor can be computed from the values of E_{11}, E_{22}, ν_{12}, and G_{12}. Using the relation

$$\frac{\nu_{12}}{E_{11}} = \frac{\nu_{21}}{E_{22}} \tag{3.1}$$

we can determine the other effective Poisson's ratio, which in this case is identical since $E_{11} = E_{22}$. We assume no axial-shear coupling and so the simplified elasticity tensor reduces to [50]

$$\mathbb{C} = \begin{bmatrix} C_{11} & C_{12} & 0 \\ C_{12} & C_{22} & 0 \\ 0 & 0 & C_{66} \end{bmatrix} \tag{3.2}$$

where

$$\begin{aligned} C_{11} &= \frac{E_{11}}{1 - \nu_{12}\nu_{21}} \\ C_{22} &= \frac{E_{22}}{1 - \nu_{12}\nu_{21}} \\ C_{12} &= \frac{\nu_{12}E_{22}}{1 - \nu_{12}\nu_{21}} \\ C_{66} &= G_{12} \end{aligned} \tag{3.3}$$

The corresponding calibrated cellular solids models are substituted in for E_{11}, E_{22}, ν_{12}, ν_{21} and G_{12} resulting in the effective elasticity tensor for the bone scaffold. As mentioned in Chapter 1, in this work we make a significant simplifying assumption: the cellular solids models and their calibration via numerical homogenization are derived for a lattice with straight, perpendicular rods. However, in the actual scaffold we consider curved rods, and we assume that at a given point in the scaffold, the effective elasticity tensor is given as above, but is rotated by ψ, the orientation of the tangent vector to the curved rod axis. Therefore, in accordance with rotation of tensors, the effective tensor is given by

$$\mathbb{C}' = \mathbf{T}^{-1}\mathbb{C}\mathbf{T} \tag{3.4}$$

where

$$\mathbf{T} = \begin{bmatrix} \cos(\psi) & \sin(\psi) & 0 \\ -\sin(\psi) & \cos(\psi) & 0 \\ 0 & 0 & 1 \end{bmatrix} \tag{3.5}$$

3.4 Optimization Problem Statements

3.4.1 Compliance minimization

The first optimization problem we solve follows a canonical mechanical optimization problem: compliance minimization subject to a volume fraction constraint. In this case, the goal is to find the stiffest scaffold possible given a maximum allowable volume fraction (i.e., a minimum allowable porosity).

$$\min_{d/l,\psi} C \coloneqq \int_{s^t} \mathbf{t}^p \cdot \mathbf{u} \; da \tag{3.6}$$

subject to:

$$V_f \coloneqq \frac{1}{|\Omega|} \int \big(1 - p(d/l)\big) \; dv \leq V_f^*, \; 0 \leq V_f^* \leq 1 \tag{3.7}$$

$$0.3 \leq \frac{d}{l} \leq \left(\frac{d}{l}\right)^* \tag{3.8}$$

where C is the structural compliance, $\mathbf{t}^p$ is the traction load applied on the traction boundary s^t, and $\mathbf{u}$ is the displacement. For our problem, $\mathbf{t}^p$ is design-independent, and we assume there are no body loads. Also, $(d/l)^*$ is an upper parameter limit set to deter regions of low porosity, found by solving the quadratic equation (3.7) for d/l with V_f^* set to a desired maximum RVE volume fraction. Without this constraint, designs will look to create high porosity in some places, but make the scaffold solid in others, which is not conducive to bone in-growth. We note that this local porosity control, in addition to the global scaffold porosity constraint, is a distinct and novel feature of our scaffold design problem as compared to, e.g., topology optimization methods. In our method, it is straightforward to impose this local porosity control because d/l is a design parameter and thus it can be directly constrained by imposing bounds on the design variables as shown above. We also impose a lower bound of 0.3 because our cellular solids models do not provide a good fit below this value, and because scaffolds with low d/l are anyways very slender scaffolds and sparse, and hence prone to mechanical instability, as explained in Chapter 2.

3.4.2 Volume fraction minimization

The second optimization problem minimizes the scaffold's volume fraction given a compliance constraint. This aims to maximize porosity while ensuring the scaffold is not stiffer than the surrounding bone. In this manner, stress shielding will be reduced while providing adequate mechanical support, and porosity will be maximized for osteointegration.

$$\min_{d/l,\psi} V_f \tag{3.9}$$

subject to:

$$C \leq C^* \tag{3.10}$$

$$0.3 \leq \frac{d}{l} \leq \left(\frac{d}{l}\right)^* \tag{3.11}$$

C^* corresponds to the compliance of the native, healthy bone that would otherwise have occupied the defect site. This value can be obtained by performing an analysis whereby the material properties for the native bone are assigned to the defect mesh. The purpose of this constraint is to render a scaffold that is at least as stiff as the native bone. The fact that we are minimizing the volume fraction, however, will render a design for which equality holds, therefore we will obtain a scaffold whose stiffness equals that of the native bone.

3.5 Sensitivity Analysis

In order to solve these optimization problems with efficient and robust gradient-based optimization methods, the sensitivities of each objective function and constraint with respect to the design parameters d/l and ψ need to be found. These resulting gradients are then passed

to the optimization method. Here we use the Method of Moving Asymptotes (MMA) [51], which is widely used in structural optimization. To obtain design sensitivities, we use the adjoint method as it only requres the solution of one pseudo-problem per function, which is more efficient than the direct method as we have a large number of design variables, namely the d/l and ψ fields. We start by differentiating the compliance from equation (3.6) as

$$DC(d) = \int_{s^t} \mathbf{t}^p \cdot D\mathbf{u} \; da \tag{3.12}$$

The analysis residual is given as

$$r(u) = 0 = -\int_{\Omega} \nabla\boldsymbol{\omega} \cdot \mathbb{C}'\nabla\mathbf{u} \; dv + \int_{s^t} \boldsymbol{\omega} \cdot \mathbf{t}^p \; da \tag{3.13}$$

where $\boldsymbol{\omega}$ are the virtual displacements (test functions), and with $\mathbb{C}'$ given by equation (3.4). Its derivative with respect to a design variable d is given by

$$D_d r(u) = 0 = -\int_{\Omega} \nabla\boldsymbol{\omega} \cdot \left[D_d\mathbb{C}'\nabla\mathbf{u} + \mathbb{C}'D_d\nabla\mathbf{u}\right] \; dv \tag{3.14}$$

where $D_d\mathbf{t}^p = \mathbf{0}$. Since the derivative of the residual is also equal to zero, it can be added to equation (3.12) without changing it

$$D_d C = \int_{s^t} \mathbf{t}^p \cdot D_d\mathbf{u} \; da - \int_{\Omega} \nabla\boldsymbol{\lambda} \cdot \left[D_d\mathbb{C}'\nabla\mathbf{u} + \mathbb{C}'D_d\nabla\mathbf{u}\right] \; dv \tag{3.15}$$

where we have replaced the test functions $\boldsymbol{\omega}$ with $\boldsymbol{\lambda}$. From the symmetries of the elasticity tensor and the commutativity of partial derivatives (Schwarz's theorem), we find that

$$\begin{aligned} \nabla\boldsymbol{\lambda} \cdot \mathbb{C}'D_d\nabla\mathbf{u} &= \mathbb{C}'^T\nabla\boldsymbol{\lambda} \cdot D_d\nabla\mathbf{u} \\ &= \mathbb{C}'\nabla\boldsymbol{\lambda} \cdot \nabla D_d\mathbf{u} \end{aligned} \tag{3.16}$$

Replacing the above into equation (3.15) and rearranging, we have

$$D_d C = -\int_{\Omega} \nabla\boldsymbol{\lambda} \cdot D_d\mathbb{C}'\nabla\mathbf{u} \; dv + \left[\int_{\Omega} \mathbb{C}'\nabla\boldsymbol{\lambda} \cdot \nabla D_d\mathbf{u} \; dv + \int_{s^t} \mathbf{t}^p \cdot D_d\mathbf{u} \; da\right] \tag{3.17}$$

We note that the portion of equation (3.17) within brackets resembles the primal analysis problem of equation (3.13) with the unknown $D_d\mathbf{u}$ taking the place of the test functions $\boldsymbol{\omega}$. Since equation (3.14) must hold for *any* test function, it must hold too for $D_d\mathbf{u}$. Therefore, by comparison to equation (3.13), it is clear that the adjoint solution $\boldsymbol{\lambda}$ must be given by $\boldsymbol{\lambda} = -\mathbf{u}$. Replacing in equation (3.17), we find that

$$D_d C = \int_{\Omega} \nabla\mathbf{u} \cdot D_d\mathbb{C}'\nabla\mathbf{u} \; dv \tag{3.18}$$

The derivative $D_d\mathbb{C}'$ is obtained from equation (3.6) using the product rule as

$$\begin{aligned} D_\psi \mathbb{C}' &= D_\psi \mathbf{T}\mathbb{C}\mathbf{T}^T + \mathbf{T}\mathbb{C}D_\psi \mathbf{T}^T \\ D_{d/l}\mathbb{C}' &= \mathbf{T}D_{d/l}\mathbb{C}\mathbf{T}^T \end{aligned} \tag{3.19}$$

where we take into account that $D_{d/l}\mathbf{T} = 0$ and $D_\psi \mathbb{C} = 0$. Replacing in equation (3.18), we find

$$D_\psi C = \int_\Omega \nabla \mathbf{u} \cdot \left[D_\psi \mathbf{T}\mathbb{C}\mathbf{T}^T + \mathbf{T}\mathbb{C}D_\psi \mathbf{T}^T \right] \nabla \mathbf{u} \, dv \tag{3.20}$$

and

$$D_{d/l} C = \int_\Omega \nabla \mathbf{u} \cdot \left[\mathbf{T}D_{d/l}\mathbb{C}\mathbf{T}^T \right] \nabla \mathbf{u} \, dv \tag{3.21}$$

where

$$D_\psi \mathbf{T} = \begin{bmatrix} -\sin(\psi) & \cos(\psi) & 0 \\ -\cos(\psi) & -\sin(\psi) & 0 \\ 0 & 0 & 0 \end{bmatrix} \tag{3.22}$$

and

$$D_{d/l}\mathbb{C} = \begin{bmatrix} D_{d/l}C_{11} & D_{d/l}C_{12} & 0 \\ D_{d/l}C_{12} & D_{d/l}C_{22} & 0 \\ 0 & 0 & D_{d/l}C_{66} \end{bmatrix} \tag{3.23}$$

Specifically, the derivative of each tensor component is

$$D_{d/l}C_{11} = D_{d/l}C_{22} = \frac{C_1 \pi E_s \left(1 - 2(\alpha - 1)\alpha^3 C_3^2 \left(\frac{d}{l}\right)^2 \nu_s^2 \right)}{8(\alpha - 1)\left(\nu_s^2 - 1\right)\left(2(\alpha - 1)\alpha^3 C_3^2 \left(\frac{d}{l}\right)^2 \nu_s^2 + 1 \right)^2} \tag{3.24}$$

$$D_{d/l}C_{12} = -\frac{C_1 C_3 \pi \alpha^2 \left(\frac{d}{l}\right) E_s \nu_s}{2\sqrt{2}\sqrt{-(\alpha - 1)\alpha}\left(\nu_s^2 - 1\right)\left(2\alpha^4 C_3^2 \left(\frac{d}{l}\right)^2 \nu_s^2 - 2\alpha^3 C_3^2 \left(\frac{d}{l}\right)^2 \nu_s^2 + 1 \right)^2} \tag{3.25}$$

and

$$D_{d/l}C_{66} = 3C_2 \alpha G_s \frac{(1 + \nu_s)}{(1 - \alpha)} \left(\frac{d}{l} \right)^2 \tag{3.26}$$

Equations (3.20) and (3.21) are discretized for use in finite elements with element-wise constant d/l and ψ.

The sensitivity analysis for the volume fraction ensues. From equations (3.7) and (2.56), we have

$$\begin{aligned} D_{d/l}V_f &= \frac{1}{|\Omega|} \int_\Omega \frac{1}{1 - \alpha} \left[\frac{\pi}{4} - \frac{4\big(1 - g(\epsilon = 1 - \alpha)\big)}{3} \left(\frac{d}{l} \right) \right] dv \\ D_\psi V_f &= 0 \end{aligned} \tag{3.27}$$

The sensitivities for equations (3.8), and (3.11) are unnecessary as they are imposed as design variable bounds.

To ensure the sensitivity analysis is correct, we compare these analytical sensitivities to

finite difference approximations. These are obtained as

$$D_i\Theta = \frac{\Theta^i_{pert} - \Theta}{\delta} \tag{3.28}$$

where Θ is either the compliance C or the volume fraction V_f, $D_i\Theta$ is its derivative with respect to the ith design variable, Θ^i_{pert} is the function value obtained by perturbing the ith design variable by δ while leaving all other design variables unperturbed, and Θ is the function value corresponding to the unperturbed design. Here, we use $\delta = 1 \times 10^{-8}$.

The finite difference sensitivity check of $D_\psi C$ finds a maximum absolute error of 1.39×10^{-4} and a maximum relative error of 2.63×10^{-5}. For $D_{d/l}C$, we find a maximum absolute error of -6.29×10^{-8} and a maximum relative error of 2.04×10^{-7}. The error is fairly small, assuring a correct derivation and computer implementation of the analytical sensitivities.

3.6 Design for Manufacturing

After solving the optimization problem, we obtain optimal ψ and d/l. These parameters do not readily translate into a design manufacturable by direct ink writing, such as the one shown in figure 1-2. In order to accomplish this, we developed an automated method to transform this set of design parameters into a design suitable for direct ink writing.

To this end, we generate a surface Φ whose level sets for a given arbitrary δ are such that the distance between the level sets Φ_{n+1} and Φ_n at $\mathbf{x}$ is the one given by $d/l(\mathbf{x})$, and the orientation of the level set $\Phi_n(\mathbf{x})$ is given by $\psi(\mathbf{x})$. In other words, we seek the function Φ such that its δ-level sets constitute the directrices of the curved rods.

Let us consider point $\mathbf{x}$ on a level set Φ_n of Φ. We desire the closest point on the adjacent level set Φ_{n+1}, which we denote by Φ_δ, to be at a distance l from $\mathbf{x}$, where l is the rod separation obtained from d/l (as we assume d is fixed by the deposition nozzle diameter), as shown in figure 3-2. That is, we want the distance between level sets (or rods) to be equal to l such that

$$l(\mathbf{x}) = ||\mathbf{x}_\delta - \mathbf{x}|| \tag{3.29}$$

From figure 3-2, the slope m can be calculated as

$$m = \frac{\big(\Phi(\mathbf{x}) + \delta\big) - \Phi(\mathbf{x})}{||\mathbf{x}_\delta - \mathbf{x}||} = \frac{\delta}{l(\mathbf{x})} \tag{3.30}$$

Because the cellular solids models were derived assuming that overlapping rods are perpendicular to each other at their intersection, we will further require that the closest point $\mathbf{x}_\delta$ to $\mathbf{x}$ lies on the normal direction of $\Phi(\mathbf{x})$. In other words, $\mathbf{x}_\delta - \mathbf{x} = \alpha\mathbf{n}$, where $\mathbf{n}$ is the normal vector and α is a real. Therefore, we consider a first-order Taylor series approximation of

$\Phi(\mathbf{x})$ along $\mathbf{n}(\mathbf{x})$, i.e.:

$$\begin{aligned}\Phi(\mathbf{x}+\alpha\mathbf{n}) &\approx \Phi(\mathbf{x}) + \nabla\Phi(\mathbf{x})\cdot\alpha\mathbf{n} \\ &= \Phi(\mathbf{x}) + \alpha\nabla\Phi(\mathbf{x})\cdot\frac{\nabla\Phi(\mathbf{x})}{|\nabla\Phi(\mathbf{x})|} \\ &= \Phi(\mathbf{x}) + \alpha|\nabla\Phi(\mathbf{x})|\end{aligned} \tag{3.31}$$

By comparing the above with equation (3.30) and noting that if $\alpha = ||\mathbf{x}_\delta - \mathbf{x}||$ then $m = |\nabla\Phi(\mathbf{x})|$, we obtain

$$|\nabla\Phi(\mathbf{x})| = \frac{\delta}{l(\mathbf{x})} \tag{3.32}$$

In other words, by controlling the magnitude of the gradient of Φ, we can get its δ-level sets to be separated at the desired distance $l(\mathbf{x})$.

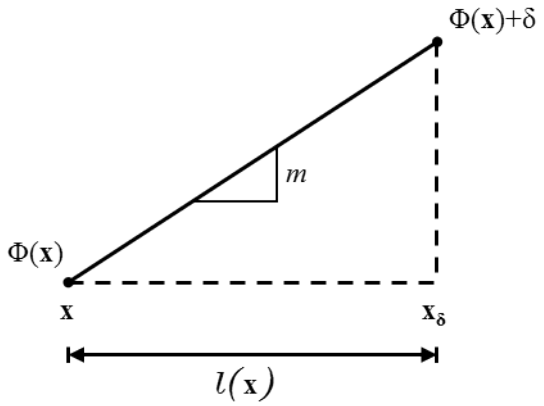

Figure 3-2: Adjacent level sets of Φ with a spacing of l from each other

In order for the level sets of Φ to also follow the rod orientation $\psi(\mathbf{x})$, we require that

$$\begin{aligned}\mathbf{n}(\mathbf{x})\cdot\mathbf{e}_1 = \frac{\nabla\Phi(\mathbf{x})\cdot\mathbf{e}_1}{|\nabla\Phi(\mathbf{x})|} &= \cos\left(\frac{\pi}{2} - \psi(\mathbf{x})\right) \\ &= \sin\left(\psi(\mathbf{x})\right)\end{aligned} \tag{3.33}$$

Since at any point $\mathbf{x}$ we have two unknowns (i.e., the components of $\nabla\Phi$) and two equations, i.e, (3.32) and (3.33), we can explicitly solve for the gradient of the level set function. Equation (3.32) is substituted into equation (3.33) to solve for the first component of the gradient as

$$\begin{aligned}\nabla\Phi(\mathbf{x})\cdot\mathbf{e}_1 &= \sin\left(\psi(\mathbf{x})\right)|\nabla\Phi(\mathbf{x})| \\ \frac{\partial\Phi(\mathbf{x})}{\partial\mathbf{x}_1} &= \frac{\sin\left(\psi(\mathbf{x})\right)\delta}{l(\mathbf{x})}\end{aligned} \tag{3.34}$$

The second component is found by first squaring equation (3.32):

$$|\nabla\Phi(\mathbf{x})|^2 = \left(\frac{\partial\Phi(\mathbf{x})}{\partial\mathbf{x}_1}\right)^2 + \left(\frac{\partial\Phi(\mathbf{x})}{\partial\mathbf{x}_2}\right)^2 = \frac{\delta^2}{l^2(\mathbf{x})} \tag{3.35}$$

We rearrange and use equation (3.34) to obtain

$$\left(\frac{\partial\Phi(\mathbf{x})}{\partial\mathbf{x}_2}\right)^2 = \frac{\delta^2}{l^2(\mathbf{x})} - \frac{\sin^2\left(\psi(\mathbf{x})\right)\delta^2}{l^2(\mathbf{x})} \tag{3.36}$$

which, after simplification, leads to

$$\left(\frac{\partial\Phi(\mathbf{x})}{\partial\mathbf{x}_2}\right)^2 = \frac{\delta^2}{l^2(\mathbf{x})}\cos^2\left(\psi(\mathbf{x})\right) \tag{3.37}$$

Therefore,

$$\nabla\Phi(\mathbf{x}) = \frac{\delta}{l(\mathbf{x})}\begin{Bmatrix}\sin(\psi(\mathbf{x}))\\ \cos(\psi(\mathbf{x}))\end{Bmatrix} \tag{3.38}$$

To obtain Φ, we first compute $\nabla\Phi$ at the nodes of the finite element mesh by averaging at each node $\mathbf{x}_j$ the element-wise separation l and orientation ψ of all the neighboring elements to that node, and using equation (3.38). Then, at each node $\mathbf{x}_j$,the value of $\Phi(\mathbf{x}_j)$ can be approximated from the values of $\Phi(\mathbf{x}_i)$ and $\nabla\Phi(\mathbf{x}_i)$ at all the nodes $\mathbf{x}_i$ connected through an element edge to $\mathbf{x}_j$ by using the first-order Taylor series

$$\Phi(\mathbf{x}_j) = \frac{1}{N_j}\left(\sum_{i=1}^{N_j}\left(\Phi(\mathbf{x}_i) + \nabla\Phi^T(\mathbf{x}_i)(\mathbf{x}_j - \mathbf{x}_i)\right)\right) \tag{3.39}$$

where N_j is the number of neighboring nodes to node j. This results in a linear system of equations

$$\mathbf{A}\Phi = \mathbf{b} \tag{3.40}$$

where $\mathbf{A}$ is the matrix whose components are given by

$$A_{ij} = \begin{cases} -1 & \text{if } i = j \\ \frac{1}{N_j} & \text{if } i \neq j \text{ and } \mathbf{x}_i \text{ is a neighbor of } \mathbf{x}_j \\ 0 & \text{otherwise} \end{cases} \tag{3.41}$$

and $\mathbf{b}$ is the vector whose component b_j is given by

$$b_j = \frac{-1}{N_j}\sum_{i=1}^{N_j}\nabla\Phi^T(\mathbf{x}_i)(\mathbf{x}_j - \mathbf{x}_i) \tag{3.42}$$

We note that this problem does not have a unique solution, since if $\Phi(\mathbf{x})$ satisfies equation (3.38), any function $\hat{\Phi}(\mathbf{x}) \coloneqq \Phi(\mathbf{x}) + ct$ will also satisfy this equation. Therefore, to obtain a unique solution, we enforce the condition $\Phi(\mathbf{x}_1) = 0$ for node 1, which eliminates the corresponding equation from the system and all coefficients associated with $\Phi(\mathbf{x}_1)$. In other words, we eliminate the first row and first column of $\mathbf{A}$.

After solving this linear system for all nodal values of Φ, its level sets can be computed as follows. For a given δ value, we linearly interpolate Φ along element edges for each element

and connect all interpolated points that satisfy $\Phi(\mathbf{x}) = \delta$ with a straight line. After doing this for all elements in the mesh, this draws a single isoline. To draw all level set contours, we repeat this polygonization process until $n\delta$ exceeds the minimum or maximum Φ present in the mesh. Once complete, all of the rod paths in one scaffold layer will be computed. To obtain the level set contours of the alternating scaffold layer, we replace equation (3.38) with

$$\nabla\Phi(\mathbf{x}) = \frac{\delta}{l(\mathbf{x})} \begin{Bmatrix} \cos(\psi(\mathbf{x})) \\ -\sin(\psi(\mathbf{x})) \end{Bmatrix} \tag{3.43}$$

and repeat the process, in essence, rotating all orientations ψ by 90°. Disambiguation may be necessary to ensure continuous contour lines result from the polygonization algorithm [52]. Once all contour lines have been calculated, we check for and remove lines with no intersection with any line in the alternating layer, as this would produce unsupported rods in the scaffold. The remaining lines are imported into a computer aided design (CAD) software. Then, the piecewise linear level set contours are replaced with smooth Bézier curves whose control points correspond to the points on the level set. Finally, a generating circle with diameter d is swept along these Bézier curves to generate the 3D rods. The process is repeated for as many layers required for the scaffold. To automate these tasks, we wrote a Python script that is executed in the open-source CAD system FreeCAD 0.16. Lastly, the final geometry is exported as an STL file to be printed by the additive manufacturing process.

3.7 Design Examples

We wrote a MATLAB program to implement the design method described in the preceding section. To validate our method, we design a scaffold with a uniaxial traction so that we can compare the result to this problem's known solution. We also performed a qualitative comparison to a cantilever beam design obtained with density-based topology optimization, using the 99-line MATLAB topology optimization code in [53]. Finally, we present examples of scaffold design for a mandibular defect.

3.7.1 Axial Loading Test

To validate our optimization procedure, we pose a problem with a well-known solution. This problem consists of the minimization of compliance of a square, uniformly-meshed scaffold subject to an axial traction loading and pin and roller boundary conditions as shown in figure 3-3a, subject to a volume fraction constraint of 0.3. The rollers on the left-hand side edge constrain translation in the horizontal axis, but allow for free deformation along the vertical axis, which prevents stresses induced by transversal deformation and guarantee a pure axial deformation state. For those conditions, we expect to get a square lattice whose rods in one layer are perfectly aligned with the loading. The design domain is discretized with 8×8 full-integration bilinear elements. The optimization converges under a lax convergence criteria (i.e., that the objective function change between consecutive iterations is less than 1×10^{-4}) after 27 iterations. The bulk material's modulus and Poisson's ratio are 100,000 and 0.3

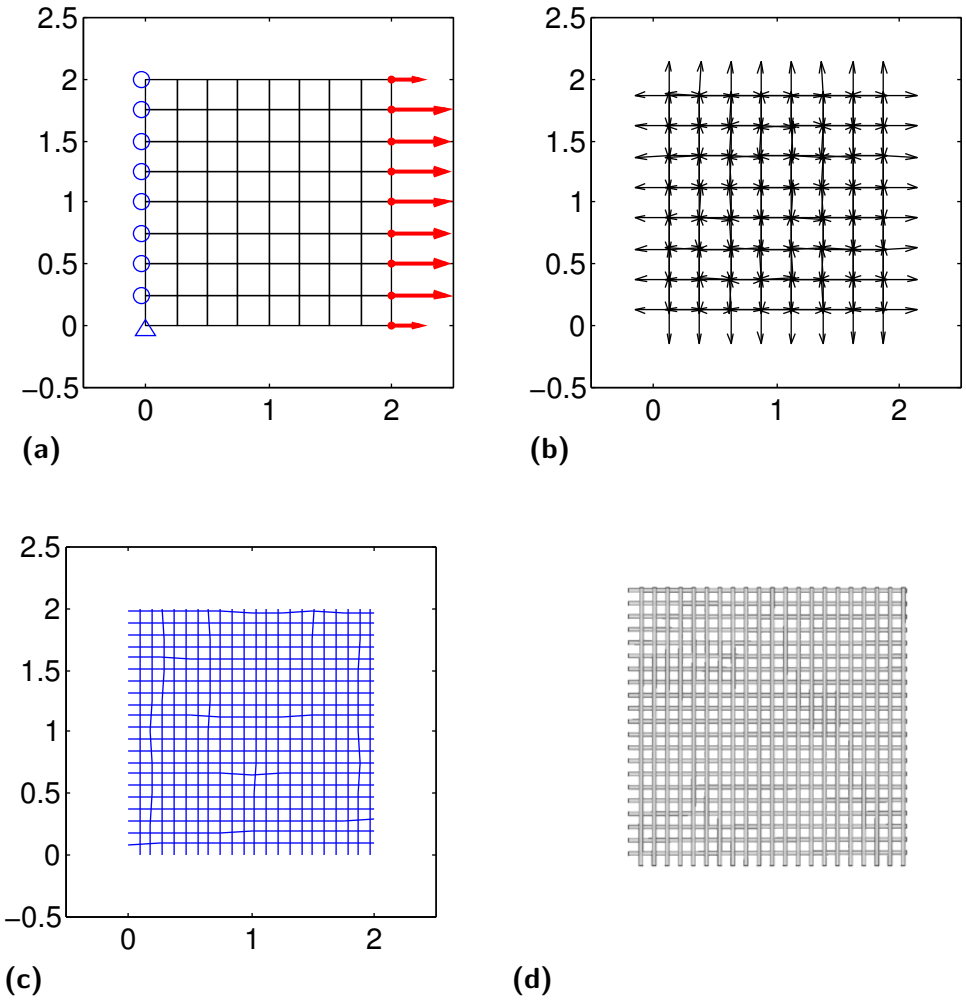

Figure 3-3: (a) The boundary conditions and loads on a square uniform mesh creating axial deformation; (b) optimized scaffold, with arrows indicating the rod direction and arrow size representing d/l; (c) projected rod layout calculated using the level set method; (d) final geometry represented in FreeCAD

respectively. The quiver plot in figure 3-3b shows the optimized ψ and d/l for the scaffold. The arrow orientations represent the rod orientations, while the arrow size is proportional to d/l. The level sets generated by the polygonization algorithm create the anticipated grid structure aligned along the axis of the load (cf. figure 3-3c). The final solid geometry is shown in figure 3-3d. As expected, the optimization procedure renders a square lattice perfectly aligned with the direction of loading.

3.7.2 Comparison to Topology Optimization Code

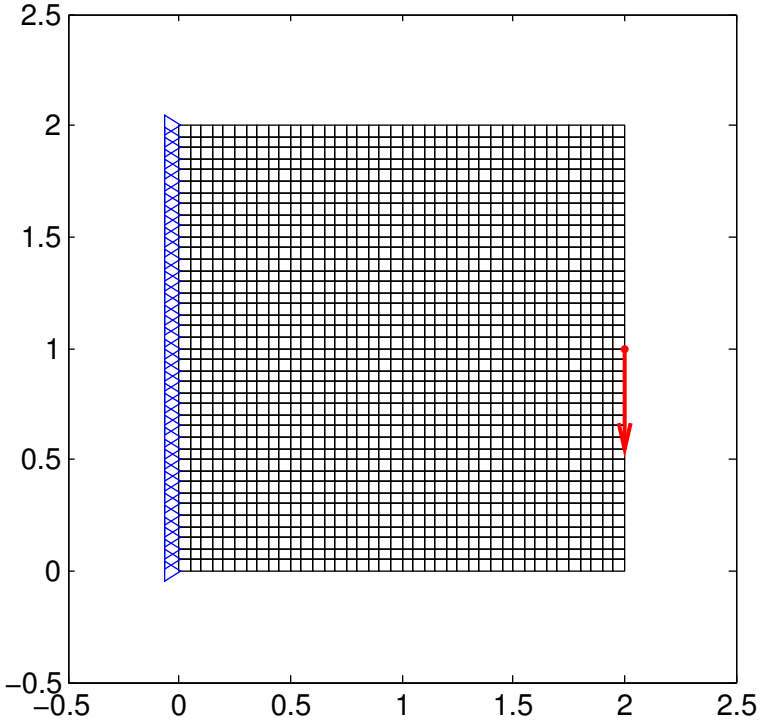

Figure 3-4: Plot shows the boundary conditions and loads on a uniformly meshed square bone scaffold

In this example, we compare the results of our procedure with those obtained by distributing a mixture of solid-void material within the design space. Specifically, we use density-based topology optimization to minimize compliance subject to a volume fraction constraint. Unlike topology optimization, however, we seek a varying mixture of material (akin to the so-called variable thickness problem) and not a pure solid/void design. Therefore, we do not use material penalization, which, in the topology optimization code [53] we achieve by setting the penalization power $p = 1$. Moreover, since artificial numerical checkerboarding does not occur in this case, we simply use a filter radius of one element size (i.e., no filter).

We design a square cantilever beam, discretized with 40×40 four-node bilinear quadrilaterals as shown in figure 3-4. The beam is encastered by fixing the vertical and horizontal displacements on all nodes on the left edge. A concentrated downward load of 1000 is applied

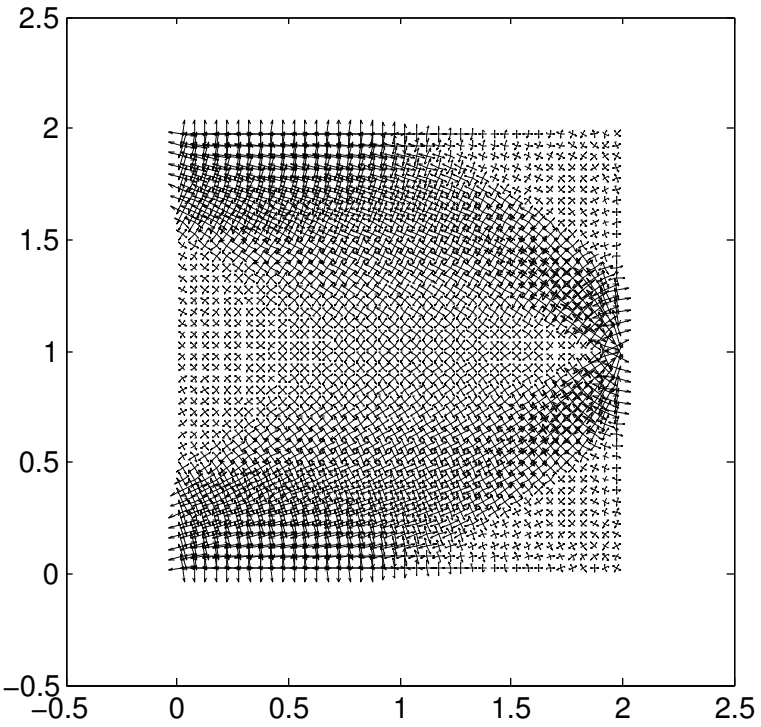

Figure 3-5: Optimized bone scaffold showing d/l and ψ for each finite element

on the midpoint of the right edge. We minimize the beam's compliance subject to a volume fraction constraint of 0.56. To be consistent with our problem formulation, we impose a lower bound on the density of 0.3, which corresponds to the lower bound on d/l of equation (3.8). We enforce a local porosity minimum of 44% by solving equation (2.56) for d/l and setting the resulting value of 0.62 as the upper bound of d/l and hence the upper bound of the density. For the scaffold, we set the overlap ratio to $\alpha = 0.15$ and use the bulk material properties described in the previous section. Henceforth, we use this value of α. The initial design for the optimization has $\psi = 0$ and $d/l = 0.1$ everywhere.

The scaffold optimization using our methodology converged after 72 iterations with a compliance of 2.098×10^2 and an objective change tolerance of 1×10^{-4}. A move limit of 0.05 is imposed on the design variables to improve convergence. The quiver plot in figure 3-5 shows the element-wise d/l and ψ for the optimal design. The solution converges monotonically, and the volume fraction constraint is satisfied as shown in figure 3-6. Figure 3-7 shows the optimal design obtained with density-based topology optimization without material penalization or filtering, which converges in 45 iterations with a compliance of 1.468×10^2 and an objective change tolerance of 1×10^{-4}. As expected, the scaffold design is more compliant than the density-based design due to the fact that the design space is more restricted as it is limited to the scaffold lattice configuration.

3.7.3 Compliance Minimization of a Mandible Implant

We now present a more realistic design example of a mandibular implant scaffold design with realistic boundary conditions seen in vivo, shown in figure 3-8. The mandible in figure 3-8 is a

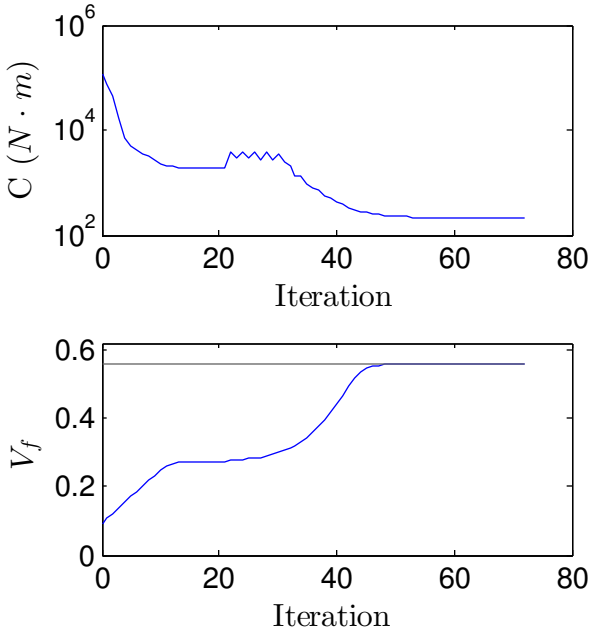

Figure 3-6: Objective function and constraint history for the short cantilever design example

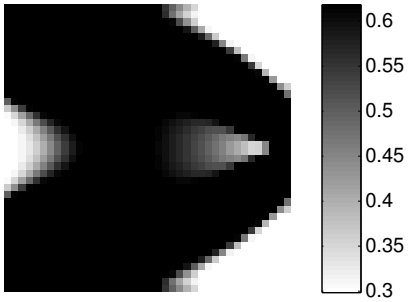

Figure 3-7: Density-based topology optimization of the short cantilever beam

2D representation adapted from [7]; we also borrow from this source all boundary conditions. The defect shape (shown in white) is a rendition of an ameloblastoma defect on the ramus of a mandible (shown in gray) [54]. The mandible and defect are meshed with 1858 bilinear four-node elements, with two additional truss elements that act as springs, shown with bold black lines. To emulate realistic boundary conditions on the jaw, the temporomandibular condyle is pinned to allow rotation but no translation (typically seen in chewing). The temporalis muscle, attached to the coronoid process, is simulated as one of the springs in the simulation. One end is pinned and the other end is fixed to the coronoid process. The masseter muscle, connected to the ramus, is simulated as the other spring and is pinned. The medial pterygoid is a redundant muscle and is omitted. The temporomandibular condyle is fixed and so the lateral pterygoid is irrelevant. The teeth are loaded evenly in the downward direction to simulate mastication. The final optimized design is load-magnitude independent for this design formulation. To determine the stiffness of the truss elements that represent

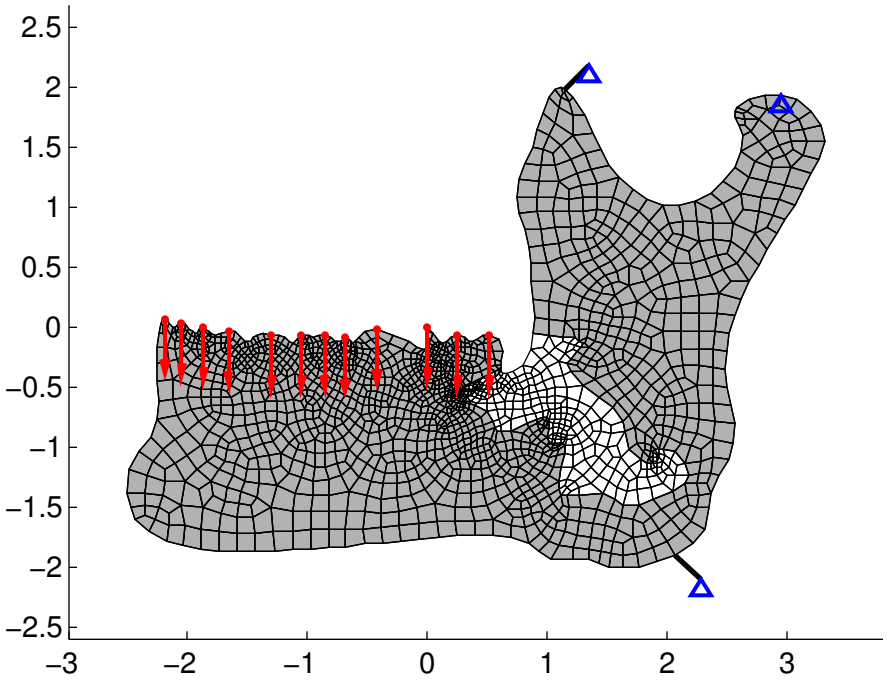

Figure 3-8: Boundary conditions for the bone scaffold (white) within a mandible (gray) example [53]

the muscles, we consider a planar truss element stiffness matrix:

$$\mathbf{K}_{truss} = \frac{EA}{L}\begin{bmatrix} c^2 & cs & -c^2 & -cs \\ cs & s^2 & -cs & -s^2 \\ -c^2 & -cs & c^2 & cs \\ -cs & -s^2 & cs & s^2 \end{bmatrix} \tag{3.44}$$

where $c = \cos(\theta)$, $s = \sin(\theta)$, and θ is the angle the truss makes with the horizontal [55]. We set E, A and L to the muscle's modulus, cross-sectional area and length respectively. The modulus E, measured by ultrasound elastography of rectus femoris muscles, is found to be approximately 12.7 kPa [56]. The masseter and temporalis mean cross-sectional areas are 4.59×10^{-4} m^2 and 4.93×10^{-4} m^2 [57], and their average lengths are 6.32×10^{-2} m and 9.00×10^{-2} m respectively [58].

We consider a scaffold made of HA, which when deposited as a colloid and sintered is found to have microporosity. Studies have shown that bulk microporous HA has a Young's modulus of 30 GPa and a Poisson's ratio of 0.25 [59], independently of micropore size. We assign material properties to the surrounding mandible bone of $E = 18.3$ GPa [60] and $\nu = 0.36$ [61]. We assume all bulk materials are isotropic and the mandible deforms under plane stress. The target porosity is 44%, which is chosen based on successful porosity values used for other mandible bone scaffolds [42]. We use this porosity to impose an upper bound of 0.62 on d/l in equation (3.8) and a volume fraction constraint of $V_f = 0.66$ on the entire scaffold. Lastly, it is important to note that only the implant's compliance is minimized, as the mandible remains intact in the design.

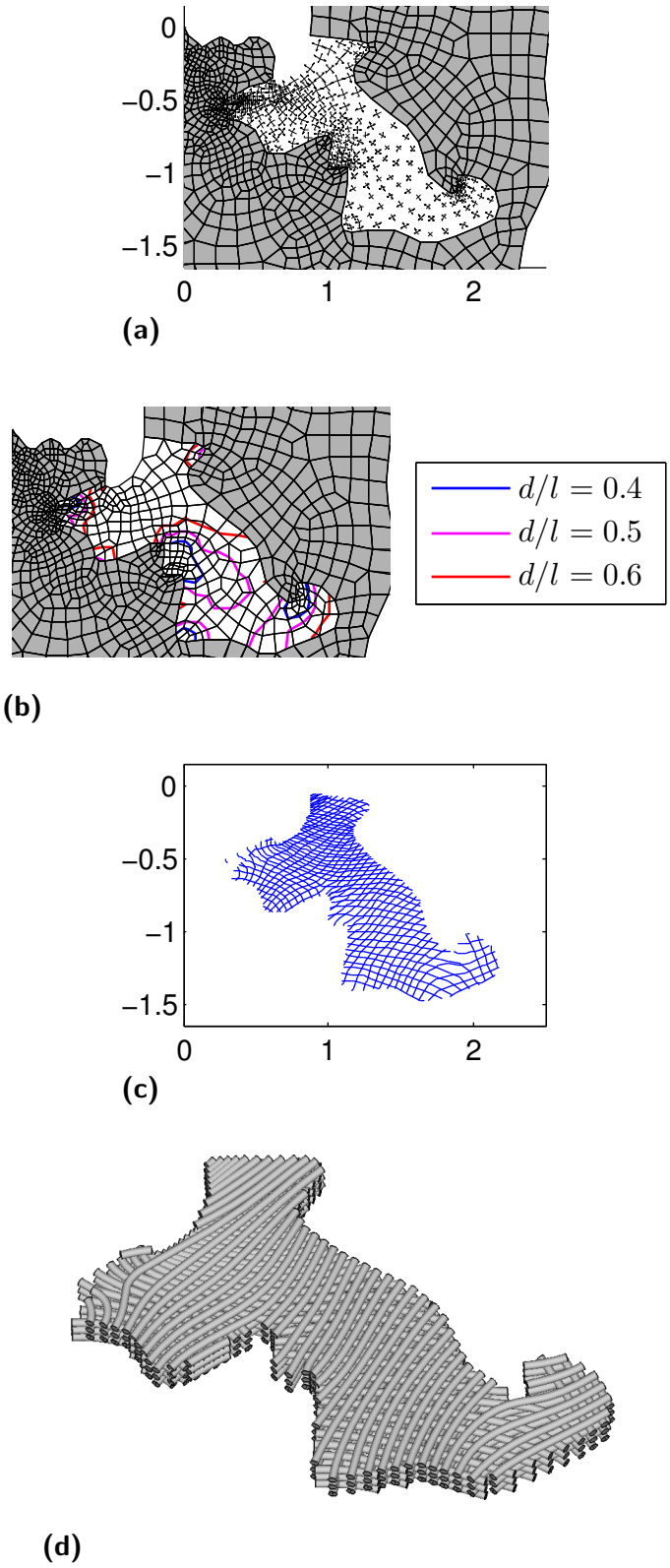

Figure 3-9: Maximal stiffness design of a mandibular implant: (a) quiver plot of optimal ψ and d/l; (b) level sets of d/l; (c) rod directrices determined by level-set method; (d) final CAD geometry.

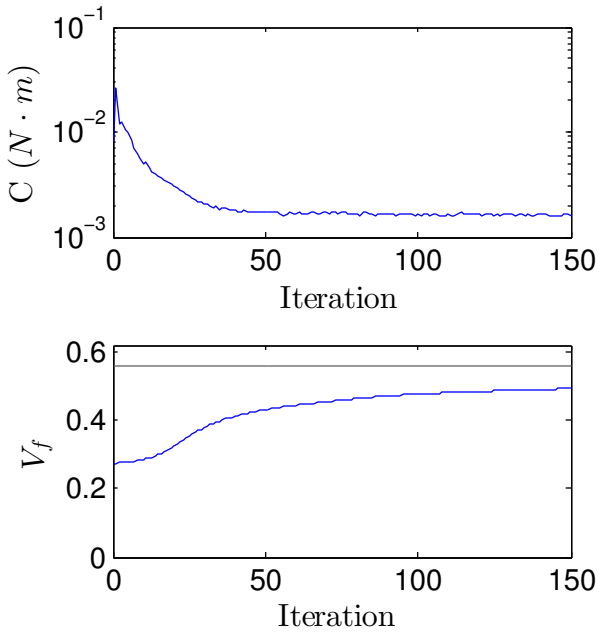

Figure 3-10: Objective and constraint function history for the stiffness example

The optimized scaffold is shown in figure 3-9a. Regions with stress concentrations or high moments, such as those nearest to the teeth, show higher d/l as expected. Rods are generally aligned along principal stress directions, in accordance with Wolff's law [8]. Denser regions in figure 3-9a do not necessarily indicate higher d/l. Instead, the mesh density is higher in regions with smaller feature sizes, giving this appearance. To depict the resulting d/l field, a polygonization algorithm was written in MATLAB to plot level set contours of d/l values averaged at the nodes, as shown in figure 3-9b. The objective function in figure 3-10 shows monotonic convergence to a compliance of $5.54 \times 10^{-4} N \cdot m$. We note that the global volume fraction constraint is not active. This is because the local volume fraction constraint imposed through the upper bound on d/l is prevalent in this example.

The result of figure 3-9a is not manufacturable. By utilizing the proposed level-set post-processing method over the mesh of nodally averaged ψ and d/l values, we obtain the rod directrices shown in figure 3-9c. Finally, the FreeCAD Python script generates the 3D-geometry shown in figure 3-9d.

3.7.4 Porosity Maximization of a Mandible Implant

In this section we revisit the mandible implant of the preceding section, but now design it for maximum porosity with a stiffness constraint. We use the same boundary conditions, loads, and bulk material properties described in the preceding section. The optimization problem, however, now uses the equations in section 3.4.2 instead of those in section 3.4.1 to define the objective function, constraint, and parameter bounds. A minimum local porosity of 44% is still imposed via upper bounds on d/l of 0.62.

The optimized scaffold is presented in figure 3-11a. It clearly contrasts that of figure 3-9a in that most of the scaffold has a low d/l. A d/l equal to the upper bound of 0.62 still occurs

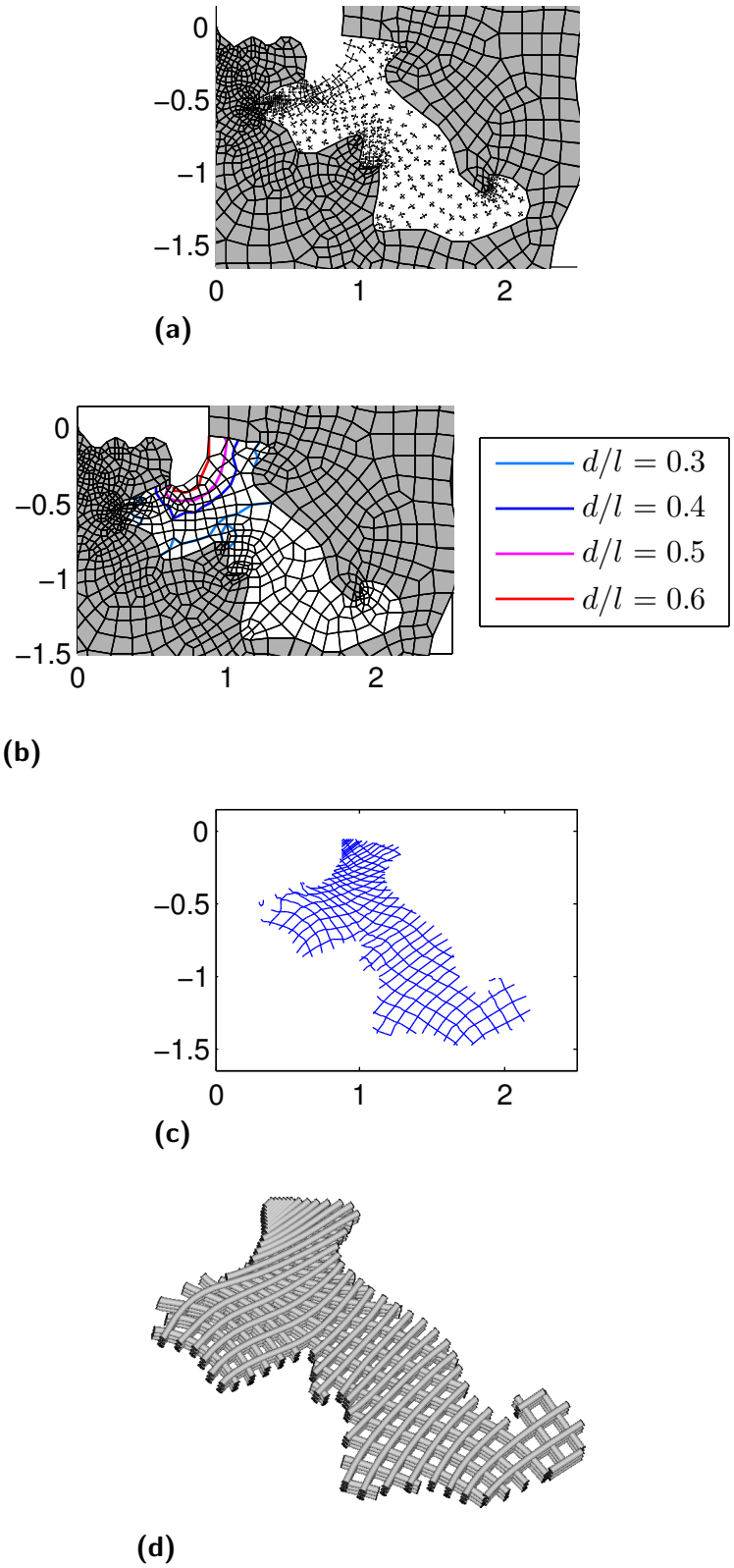

Figure 3-11: Maximal porosity design of a mandibular implant: (a) quiver plot of optimal ψ and d/l; (b) level sets of d/l; (c) rod directrices determined by level-set method; (d) final CAD geometry.

in regions of stress concentration found in the anterior edge of the ramus angle, as can be seen in figure 3-11b. The rest of the scaffold has a d/l that nears the lower bound of 0.3.

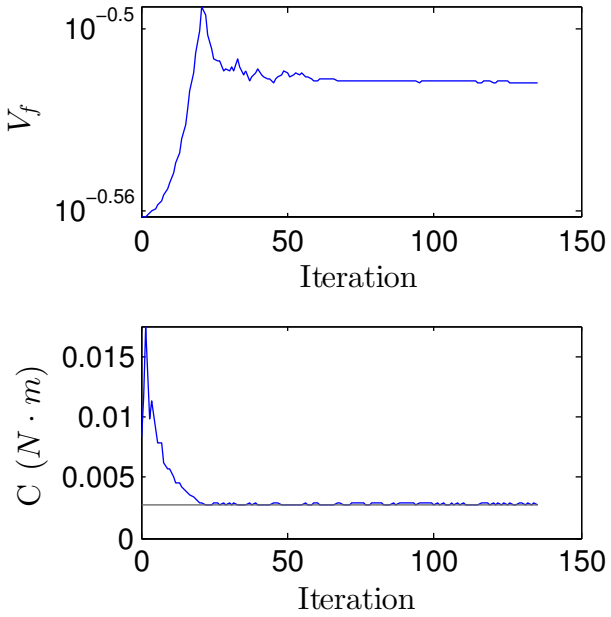

Figure 3-12: Objective and constraint function history for the maximal porosity example

The objective function history in figure 3-12 increases at first, due to the fact that the compliance constraint is violated in the initial design. After the constraint is satisfied, the volume fraction is consistently decreased. With a porosity nearing 70% yet still exhibiting the same compliance as that of the natural bone it is replacing, the bone scaffold shown in figure 3-11a is superior to the scaffold resulting from minimization of compliance, which is too stiff and too dense. Following the same procedure outlined before, we obtain the print path shown in figure 3-11c and use it to generate the final geometry in figure 3-11d. The FreeCAD geometry representation of the optimized scaffold is readily converted to STL format for additive manufacturing. In this case, we utilize the largest nozzle gauge (i.e., 18) considered for use in the direct ink write process in reference [28] to enhance printability. Using the Formlabs Form 1+ SLA printer, we fabricated a prototype of the scaffold shown in figure 3-13.

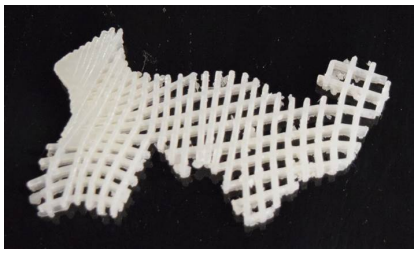

Figure 3-13: Final geometry constructed by the Formlabs Form 1+

3.8 Discussion

The quiver plots of ψ and d/l indicate that rods are oriented along principal stresses as predicted by Wolff's law [8, 23]. The lattice is stiffest axially along the rods, so that minimal deflection occurs when the rods locally align along axes of major deflection. Under the minimum compliance formulation, it was found that 45% of finite elements attain the minimum acceptable porosity, while under the minimum volume fraction formulation, 85% of finite elements were at maximum acceptable porosity. This is intuitive since a minimum compliance demands a scaffold with the stiffest possible geometry configuration. For example, without a volume fraction constraint, all d/l values would tend to the parameter upper bound 0.62. Since sintered HA is stiffer than bone, the minimum volume fraction formulation, having lesser stiffness requirements, only places stiffness (i.e., high d/l, dense RVEs) in critical areas such as those with high moment or stress concentration, while the lesser load-bearing regions have maximum porosity. The latter formulation is more adequate for bone scaffold design since it has the same compliance as the surrounding bone yet renders a high porosity, nearing 70%, that promotes cell seeding, angiogenesis, nutrient and waste transport, osteointegration, and osteoconduction.

Chapter 4

Conclusion

4.1 Contributions to Bone Scaffold Technology

We presented a novel computational methodology to design curvilinear lattice scaffolds for solid freeform fabrication. In particular, it is the first automated optimization process tailored to ceramic bone scaffolds fabricated via direct ink write. Our method gains efficiency and robustness by employing 'offline' cellular solids models thereby circumventing expensive 'online' numerical homogenization. Also novel is our level-set post-processing formulation, which translates the optimal design into a solid model suitable for manufacturing in an automated manner.

4.2 Future Research

This problem was simplified using plane stress and so defects are limited to flat bones. For more realistic results and broadened application, our method should be extended to a 3-dimensional problem. To further simplify, HA was assumed to be isotropic. HA generally expresses preferential grain growth during sintering that imparts anisotropic behavior and it exhibits microporosity when deposited as a rod. Future simulations could take these factors into account to make a more accurate solution.

To improve bone scaffold design, alternate optimization problems could be explored to improve the bone scaffold properties. One such problem, posed by [46], is the minimization of the least square error between desired and actual stiffness tensors subject to porosity constraints. Moreover, important buckling, compressive strength, and bone adaptation considerations must be incorporated in the design. In particular, the bone adaption problem would be paramount to predicting long term efficacy of the scaffold in vivo.

To improve upon patient tailorability, it is recommended that the patient defect is scanned by computed tomography (CT). Then mechanical testing of these scaffolds at each parameter level would validate the homogeneous properties of the cellular solid models and provide an empirical data set for which to calibrate the cellular solids. Ultimately, we would want to test the scaffold efficacy in vivo.

Bibliography

[1] A. S. Brydone, D. Meek, and S. Maclaine. Bone grafting, orthopaedic biomaterials, and the clinical need for bone engineering. *Proc. Inst. Mech. Eng. H J. Eng. Med.*, 224(12):1329–1343, 2010.

[2] R. Dimitriou, E. Jones, D. McGonagle, and P. V. Giannoudis. Bone regeneration: current concepts and future directions. *BMC medicine*, 9(16):66–76, 2011.

[3] S. S. Liao, F. Z. Cui, W. Zhang, and Q. L. Feng. Hierarchically biomimetic bone scaffold materials: Nano-ha/collagen/pla composite. *Journal of Biomedical Materials Research Part B: Applied Biomaterials*, 69B(2):158–165, 2004.

[4] Randal R. Betz. Limitations of autograft and allograft: new synthetic solutions. *Orthopedics*, 25(5):561–570, 2002.

[5] Liliana Polo-Corrales, Magda Latorre-Esteves, and Jaime E Ramirez-Vick. Scaffold design for bone regeneration. *Journal of nanoscience and nanotechnology*, 14(1):15–56, 2014.

[6] William W. Tomford. Bone allografts: past, present and future. *Cell and Tissue Banking*, 1(2):105–109, 2000.

[7] Henry Gray and Warren H. Lewis. *Anatomy of the Human Body*. Lea & Febiger 1918, Philadelphia, 20th edition, 2000.

[8] J. Wolff. *Das Gesetz der Transformation der Knochen*. Hirchwild, Berlin, 1892.

[9] T. Albrektsson and C. Johansson. Osteoinduction, osteoconduction and osseointegration. *European Spine Journal*, 10(2):96–101, 2001.

[10] Matthias Schieker, Hermann Seitz, Inga Drosse, Sebastian Seitz, and Wolf Mutschler. Biomaterials as scaffold for bone tissue engineering. *European Journal of Trauma*, 32(2):114–124, 2006.

[11] Direct metal laser sintering materials. https://www.stratasysdirect.com/materials/direct-metal-laser-sintering/. Accessed: 2016-08-24.

[12] Kelly Alvarez and Hideo Nakajima. Metallic scaffolds for bone regeneration. *Materials*, 2(3):790–832, 2009.

[13] X. Liu and P. X. Ma. Polymeric Scaffolds for Bone Tissue Engineering. *Annals of Biomedical Engineering*, 32(3):477–486, 2004.

[14] Zeeshan Sheikh, Shariq Najeeb, Zohaib Khurshid, Vivek Verma, Haroon Rashid, and Michael Glogauer. Biodegradable materials for bone repair and tissue engineering applications. *Materials*, 8(9):5744–5794, 2015.

[15] J. A. Lewis, J. E. Smay, J. Stuecker, and J. Cesarano. Direct ink writing of three-dimensional ceramic structures. *Journal of the American Ceramic Society*, 89(12):3599–3609, 2006.

[16] B. D. Ratner, A. S. Hoffman, F. J. Schoen, and J. E. Lemons. *Biomaterials Science*. Elsevier Academic Press, New York, 2004.

[17] David J. Hoelzle, Andrew G. Alleyne, and Amy J. Wagoner Johnson. Micro-robotic deposition guidelines by a design of experiments approach to maximize fabrication reliability for the bone scaffold application. *Acta Biomaterialia*, 4(4):897–912, 2008.

[18] Chengde Gao, Youwen Deng, Pei Feng, Zhongzheng Mao, Pengjian Li, Bo Yang, Junjie Deng, Yiyuan Cao, Cijun Shuai, and Shuping Peng. Current progress in bioactive ceramic scaffolds for bone repair and regeneration. *International Journal of Molecular Sciences*, 15(3):4714–4732, 2014.

[19] Yuhang Chen, Shiwei Zhou, and Qing Li. Microstructure design of biodegradable scaffold and its effect on tissue regeneration. *Biomaterials*, 32(22):5003–5014, 2011.

[20] Stefan Sturm, Shiwei Zhou, Yiu-Wing Mai, and Qing Li. On stiffness of scaffolds for bone tissue engineeringa numerical study. *Journal of Biomechanics*, 43(9):1738–1744, 2010.

[21] Joseph P. Vacanti Robert Langer. Tissue engineering. *Science*, 260(5110):920–926, 1993.

[22] Susmita Bose, Mangal Roy, and Amit Bandyopadhyay. Recent advances in bone tissue engineering scaffolds. *Trends in Biotechnology*, 30(10):546–54, 2012.

[23] L. Gibson and M. Ashby. *Cellular Solids: Structure and Properties*. Cambridge University Press, London, 1999.

[24] P. Lichte, H.C. Pape, T. Pufe, P. Kobbe, and H. Fischer. Scaffolds for bone healing: Concepts, materials and evidence. *Injury*, 42(6):569–573, 2011. Bone Regeneration in the 21st Century.

[25] D. W. Hutmacher, J. T. Schantz, C. X. F. Lam, K. C. Tan, and T. C. Lim. State of the art and future directions of scaffold-based bone engineering from a biomaterials perspective. *Journal of Tissue Engineering and Regenerative Medicine*, 1(4):245–260, 2007.

[26] Shunsuke Fujibayashi, Masashi Neo, Hyun-Min Kim, Tadashi Kokubo, and Takashi Nakamura. Osteoinduction of porous bioactive titanium metal. *Biomaterials*, 25(3):443–450, 2004.

[27] Huipin Yuan, Hugo Fernandes, Pamela Habibovic, Jan de Boer, Ana MC Barradas, Ad de Ruiter, William R Walsh, Clemens A van Blitterswijk, and Joost D de Bruijn. Osteoinductive ceramics as a synthetic alternative to autologous bone grafting. *Proceedings of the National Academy of Sciences*, 107(31):13614–13619, 2010.

[28] J. Norato and A. Wagoner Johnson. A computational and cellular solids approach to the stiffness-based design of bone scaffolds. *J. Biomech. Eng.*, 133(9), 2011.

[29] R. D. Farahani, K. Chizari, and D. Therriault. Three-dimensional printing of freeform helical microstructures: a review. *Nanoscale*, 6(18):10470–10485, 2014.

[30] L. Gibson. Biomechanics of cellular solids. *J. Biomech.*, 38(3):377–399, 2005.

[31] S. J. Hollister and N. Kikuchi. A comparison of homogenization and standard mechanics analyses for periodic porous composites. *Computational Mechanics*, 10(2):73–95, 1992.

[32] Martin Philip Bendsøe and Ole Sigmund. *Topology Optimization: Theory, Methods and Applications*. Springer-Verlag, New York, 2003.

[33] Alexander L Kalamkarov, Igor V Andrianov, and Vladyslav V. Danishevskyy. Asymptotic Homogenization of Composite Materials and Structures. *Applied Mechanics Reviews*, 62(3):1–20, 2009.

[34] Zheng Yuan and Jacob Fish. Toward realization of computational homogenization in practice. *International Journal for Numerical Methods in Engineering*, 73(3):361–380, 2008.

[35] Erik Andreassen and Casper Schousboe Andreasen. How to determine composite material properties using numerical homogenization. *Computational Materials Science*, 83(1):488–495, 2014.

[36] Donald W. Marquardt. An algorithm for least-squares estimation of nonlinear parameters. *Journal of the Society for Industrial and Applied Mathematics*, 11(2):431–441, 1963.

[37] W. C. Young and Richard G. Budynas. *Roark's Formulas for Stress and Strain*. McGraw-Hill, New York, 7th edition, 2002.

[38] J. Norato, R. Haber, D. Tortorelli, and M. P. Bendsøe. A geometry projection method for shape optimization. *International Journal for Numerical Methods in Engineering*, 60(14):2289–2312, 2004.

[39] Wolfgang Bangerth, Timo Heister, Luca Heltai, Guido Kanschat, Martin Kronbichler, Matthias Maier, and Bruno Turcksin. The deal.ii library, version 8.3. *Archive of Numerical Software*, 4(100):1–11, 2016.

[40] L. Dalcin, R. Paz, and M. Storti. Mpi for python. *Journal of Parallel and Distributed Computing*, 65(9):1108–1115, 2005.

[41] J. Yang. Development about composite homogenization in static and in dynamic - application to UD composite materials. Master's thesis, Ecole Centrale de Nantes, 2010.

[42] Vassilis Karageorgiou and David Kaplan. Porosity of 3D biomaterial scaffolds and osteogenesis . *Biomaterials*, 26(27):5474–5491, 2005.

[43] Toshihiro Sugiyama, Lee B Meakin, William J Browne, Gabriel L Galea, Joanna S Price, and Lance E Lanyon. Bones' adaptive response to mechanical loading is essentially linear between the low strains associated with disuse and the high strains associated with the lamellar/woven bone transition. *Journal of Bone and Mineral Research*, 27(8):1784–1793, 2012.

[44] Marta R. Dias, Jose M. Guedes, Colleen L. Flanagan, Scott J. Hollister, and Paulo R. Fernandes. Optimization of scaffold design for bone tissue engineering: A computational and experimental study. *Medical Engineering & Physics*, 36(4):448–457, 2014.

[45] S.J. Hollister, R.D. Maddox, and J.M. Taboas. Optimal design and fabrication of scaffolds to mimic tissue properties and satisfy biological constraints. *Biomaterials*, 23(20):4095–4103, 2002.

[46] Cheng Yu Lin, Noboru Kikuchi, and Scott J. Hollister. A novel method for biomaterial scaffold internal architecture design to match bone elastic properties with desired porosity. *Journal of Biomechanics*, 37(5):623–636, 2004.

[47] H. Kang, C. Lin, and S. J. Hollister. Topology optimization of three dimensional tissue engineering scaffold architectures for prescribed bulk modulus and diffusivity. *Structural and Multidisciplinary Optimization*, 42(4):633–644, 2010.

[48] Antonio Boccaccio, Antonio Emmanuele Uva, Michele Fiorentino, Luciano Lamberti, and Giuseppe Monno. A mechanobiology-based algorithm to optimize the microstructure geometry of bone tissue scaffolds. *International Journal of Biological Sciences*, 12(1):1–17, 2016.

[49] Przemysław Makowski and Wacław Kuś. Optimization of bone scaffold structures using experimental and numerical data. *Acta Mechanica*, 227(1):139–149, 2016.

[50] Michael W. Lai, David Rubin, and Erhard Krempl. *Introduction to Continuum Mechanics*. Elsevier, New York, 4th edition, 2010.

[51] Krister Svanberg. The method of moving asymptotesa new method for structural optimization. *International journal for numerical methods in engineering*, 24(2):359–373, 1987.

[52] DA Rajon and WE Bolch. Marching cube algorithm: review and trilinear interpolation adaptation for image-based dosimetric models. *Computerized Medical Imaging and Graphics*, 27(5):411–435, 2003.

[53] O. Sigmund. A 99 line topology optimization code written in Matlab. *Structural and Multidisciplinary Optimization*, 21(2):120–127, 2001.

[54] George Sandor. Tissue engineering of bone: clinical observations with adipose-derived stem cells, resorbable scaffolds, and growth factors. *Annals of Maxillofacial Surgery*, 2(1):8–11, 2012.

[55] Robert D. Cook, David S. Malkus, Michael E. Plesha, and Robert J. Witt. *Concepts and Applications of Finite Element Analysis*. John Wiley & Sons, 2007.

[56] B. C. W. Kot, Z. J. Zhang, A. W. C. Lee, V. Y. F. Leung, and S. N. Fu. Elastic modulus of muscle and tendon with shear wave ultrasound elastography: variations with different technical settings. *PLoS ONE*, 7(8):e44348, 2012.

[57] Viviana Toro-Ibacache, Victor Zapata Munoz, and Paul O'Higgins. The predictability from skull morphology of temporalis and masseter muscle cross-sectional areas in humans. *The Anatomical Record*, 298(7):1261–1270, 2015.

[58] Mohammed Faouzi Azaroual, Meriem Fikri, Redouan Abouqal, Hicham Benyahya, and Fatima Zaoui. Relationship between dimensions of muscles of mastication (masseter and lateral pterygoid) and skeletal dimensions: Study of 40 cases. *International Orthodontics*, 12(1):111–124, 2014.

[59] Jacqueline M. Cordell, Michelle L. Vogl, and Amy J. Wagoner Johnson. The influence of micropore size on the mechanical properties of bulk hydroxyapatite and hydroxyapatite scaffolds . *Journal of the Mechanical Behavior of Biomedical Materials*, 2(5):560–570, 2009.

[60] W.-J. Seong, U.-K. Kim, J.Q. Swift, Y.-C. Heo, J.S. Hodges, and C.-C. Ko. Elastic properties and apparent density of human edentulous maxilla and mandible. *International Journal of Oral and Maxillofacial Surgery*, 38(10):1088–1093, 2009.

[61] R. Shahar, P. Zaslansky, M. Barak, A.A. Friesem, J.D. Currey, and S. Weiner. Anisotropic poisson's ratio and compression modulus of cortical bone determined by speckle interferometry. *Journal of Biomechanics*, 40(2):252–264, 2007.

[62] Z. Fang, C. Yan, W. Sun, A. Shokoufandeh, and W. Regli. Homogenization of heterogeneous tissue scaffold: A comparison of mechanics, asymptotic homogenization, and finite element approach. *Applied Bionics and Biomechanics*, 2(1):17–29, 2005.